INVESTIGATION OF MECHANICAL AND THERMAL PROPERTIES OF SINTERED BAUXITE AND SAND PARTICLES AS HEAT TRANSFER AND STORAGE MEDIA

A THESIS SUBMITTED TO
THE GRADUATE SCHOOL OF NATURAL AND APPLIED SCIENCES
OF
MIDDLE EAST TECHNICAL UNIVERSITY

BY

ZEYNEP UYKUN

IN PARTIAL FULFILLMENT OF THE REQUIREMENTS
FOR
THE DEGREE OF MASTER OF SCIENCE
IN
MECHANICAL ENGINEERING

FEBRUARY 2021

Approval of the thesis:

INVESTIGATION OF MECHANICAL AND THERMAL PROPERTIES OF SINTERED BAUXITE AND SAND PARTICLES AS HEAT TRANSFER AND STORAGE MEDIA

submitted by **ZEYNEP UYKUN** in partial fulfillment of the requirements for the degree of **Master of Science in Mechanical Engineering Department, Middle East Technical University** by,

Prof. Dr. Halil Kalıpçılar
Dean, Graduate School of **Natural and Applied Sciences** ____________

Prof. Dr. M.A. Sahir Arıkan
Head of Department, **Mechanical Engineering** ____________

Prof. Dr. İlker Tarı
Supervisor, **Mechanical Engineering, METU** ____________

Prof. Dr. Derek K. Baker
Co-supervisor, **Mechanical Engineering, METU** ____________

Examining Committee Members:

Prof. Dr. Derek K. Baker
Mechanical Engineering, METU ____________

Prof. Dr. İlker Tarı
Mechanical Engineering, METU ____________

Assoc. Prof. Dr. Özgür Bayer
Mechanical Engineering, METU ____________

Prof. Dr. Tuba Okutucu Özyurt
Energy Institute, ITU ____________

Assist. Prof. Dr. Mehdi Mehrtash
Energy Systems Engineering, Atılım University ____________

Date: 11.02.2021

I hereby declare that all information in this document has been obtained and presented in accordance with academic rules and ethical conduct. I also declare that, as required by these rules and conduct, I have fully cited and referenced all material and results that are not original to this work.

Name, Surname: Zeynep Uykun

Signature :

ABSTRACT

INVESTIGATION OF MECHANICAL AND THERMAL PROPERTIES OF SINTERED BAUXITE AND SAND PARTICLES AS HEAT TRANSFER AND STORAGE MEDIA

Uykun, Zeynep
M.S., Department of Mechanical Engineering
Supervisor: Prof. Dr. İlker Tarı
Co-Supervisor: Prof. Dr. Derek K. Baker

February 2021, 100 pages

Solid particles have gained an attraction in recent years to be used as a heat transfer and storage medium that can be integrated into various thermal power plants. Particles operate in a closed-loop cycle in the power plants such as Concentrating Solar Power (CSP); firstly, they are heated up in the receiver then carried to the storage system and they discharge their energy to the thermodynamic-cycle. Discrete Element Method (DEM) has been gaining importance for modeling particle-based heat transfer and storage systems such as CSP and its components. DEM predicts the bulk particle behaviour more accurately than continuum models. To properly model the particles as a bulk, exact individual particle properties should be inputted to DEM models. Properties of candidate particles that are input to DEM are investigated in this study. Two of the popular candidate particles which are CarboHSP 40/70 and sand are examined in terms of mechanical and thermal characteristics. Particle-particle and particle-wall rolling and sliding frictions and restitution coefficients of candidate particles are investigated. The inclined plane test was performed for the investigation of the particle-wall friction coefficient. The discharged test was utilized for the calibration of other parameters. Inter-particle friction coefficients were calibrated by Angle of Repose (AOR) and discharged mass measurement. A new useful calibration method for the investigation of the restitution coefficient is presented. This method suggests the scattering measurement of particles after discharge. Particle-wall and inter-particle restitution coefficients of examined particles are investigated by utilizing this method. Solid particles are in a thermal cycle as heat transfer and storage medium in related systems by heating up and cooling down. To meet this case, particles were cycled in a furnace many times from room temperature to 700 °C and calibration tests with repeated with cycled particles. Also, the discharge test was repeated with hot particles up to 600 °C. Particle properties, as well as particle resistance, were checked in this way. Hot Disk measurement device was used for thermal characterization of the particles from room temperature to elevated temperatures. Sensor bias was corrected at high-temperature measurements with Mica sensor to avoid overestimation of properties. Specific heat capacity and bulk thermal conductivity of the candidate particles were measured and reported.

Keywords: particle-based heat transfer medium, particle TES, DEM, particle properties, calibration, Hot Disk, CSP

ÖZ

ISI TRANSFERİ VE DEPOLAMA ORTAMI OLAN SİNTERLENMİŞ BOKSİT VE KUM PARÇACIKLARININ MEKANİK VE TERMAL ÖZELLİKLERİNİN İNCELENMESİ

Uykun, Zeynep

Yüksek Lisans, Makina Mühendisliği Bölümü

Tez Yöneticisi: Prof. Dr. İlker Tarı

Ortak Tez Yöneticisi: Prof. Dr. Derek K. Baker

Şubat 2021 , 100 sayfa

Son yıllarda katı parçacıkların termal enerji santrallerinde ısı transferi ve depolaması ortamı olarak kullanılması önem kazanmıştır. Katı parçacıklar Yoğunlaştırılmış Güneş enerjisi (YGE) gibi santrallerde kapalı döngüde çalışırlar; önce alıcıda ısınırlar, ardından depolama sistemine taşınırlar ve enerjilerini termodinamik-döngüye boşaltırlar. Günümüzde YGE sistemleri ve bileşenleri gibi parçacık tabanlı ısı transfer ve depolaması ortamlarının Ayrık Eleman Yöntemi (AEY) ile modellenmesi önem kazanmıştır. AEY parçacıkların yığın davranışını sürekli modellerden daha doğru tahmin eder. Parçacıkları bir yığın olarak doğru bir şekilde modellemek için, doğru parçacık özellikleri AEY modellerine girdi olmalıdır. Bu çalışmada YGE sistemlerinde kullanılmaya aday parçacıkların AEY modellerine girdi olacak özellikleri araştırılmıştır. Popüler aday parçacıklardan ikisi olan CarboHSP 40/70 ve kum, mekanik ve ısıl özellikler açısından incelenmiştir. Partikül-partikül ve partikül-duvar dönme ve kayma sürtünmeleri ve aday partiküllerin geri sıçrama katsayıları incelenmiştir. Parçacık-duvar sürtünme katsayısının araştırılması için eğimli düzlem testi yapılmıştır. Diğer parametrelerin kalibrasyonu için boşalma testi kullanılmıştır. Parçacıklar arası sürtünme katsayıları, Doğal Kayma Açısı (DKA) ve boşalan kütle ölçümü kullanarak kalibre edilmiştir. Geri sıçrama katsayısının incelenmesi için yeni bir kullanışlı kalibrasyon yöntemi sunulmuştur. Bu yöntem, deşarjdan sonra parçacıkların saçılma ölçümünü önermektedir. İncelenen partiküllerin partikül duvarı ve partiküller arası geri sıçrama katsayıları bu yöntem kullanılarak kalibre edilmiştir. Katı parçacıklar ısı transferi ve depolaması olarak kullanıldıkları sistemlerde ısınıp soğuyarak bir termal döngü içindedirler. Bu durumu karşılamak için parçacıklar bir fırında oda sıcaklığından 700 °C'ye pek çok kere termal çevrime uğratıldı ve bu parçacıklarla kalibrasyon testleri yapılmıştır. Ayrıca 600°C'ye kadar sıcak partiküllerle deşarj testi tekrarlanmıştır. Partikül özellikleri ve partikül direnci bu şekilde kontrol edilmiştir. Partiküllerin oda sıcaklığından yüksek sıcaklıklara kadar olan ısıl karakterizasyonu için Sıcak Disk ölçüm cihazı kullanılmıştır. Mika sensörüyle yüksek sıcaklık ölçümlerinde özellik değerlerinin olduğundan yüksek tahmin edilmesini önlemek için sensör sapması düzeltilmiştir. Aday parçacıkların özgül ısı kapasitesi ve yığın ısıl iletkenliği ölçülerek rapor edilmiştir.

Anahtar Kelimeler: parçacıklı ısı transferi ortamı, parçacıklı termal enerji depolama, Ayrık Elemanlar Methodu, parçacık özellikleri, kalibrasyon, Sıcak Disk, Yoğunlaştırılmış Güneş Enerjisi

to my family

ACKNOWLEDGMENTS

I would like to express my sincere gratitude to Prof. Dr. İlker Tarı and Prof. Dr. Derek Baker for their guidance and continuous supports, the opportunities they offer and contributions throughout my study. Their broad vision encouraged me to learn more in this field.

I would also like to thank Evan Johnson and Serdar Hiçdurmaz for sharing their knowledge and experience with me and insightful discussions about my thesis. I learned so much from them.

Also, I am thankful to Mustafa Yalçın for his precious help in laboratory work.

Finally, I would like to thank my family for their endless support.

TABLE OF CONTENTS

LIST OF TABLES

TABLES

LIST OF FIGURES

FIGURES

NOMENCLATURE

ABBREVIATIONS

AOR	Angle of repose
CSP	Concentrated solar power
CFD	Computational fluid dynamics
DEM	Discrete element method
DSC	Differential scanning calorimeter
EPDS2	Elastic plastic spring dashpot
TES	Thermal energy storage
TPS	Transient plane source
ZBS	Zehner-Bauer-Schlünder

LIST OF SYMBOLS

F	Force, N
F_t	Tangential force, N
F_n	Normal force, N
$F_{external}$	Extarnal force, N
$F_{fluid-particle}$	Interaction force between fluid and particle, N
$F_{particle-particle}$	Interaction force between two particles, N
M_t	Total moment, $\mathrm{N\,m}$
M_r	Rolling resistance moment $\mathrm{N\,m}$
M_k	Spring moment, $\mathrm{N\,m}$
M_d	Spring damping moment, $\mathrm{N\,m}$
M_M	Mobilization moment, $\mathrm{N\,m}$
$\Delta\theta$	Incremental relative rotation between two particles, rad

V	Linear velocity, $\mathrm{m/s}$
ω	Angular velocity, $\mathrm{rad/s}$
x	Linear particle position, m
θ	Angular particle position, rad
R	Particle radius, m
N_{verlet}	Velocity verlet time step, sec
Δt	Constant time step, sec
Δt_r	Rayleigh time step, sec
Δt_h	Hertz time step, sec
V_{max}	Maximum particle velocity, $\mathrm{m/s}$
V_{ij}	Relative velocity of particles, $\mathrm{m/s}$
k	Elastic stiffness constants, $\mathrm{N/m}$
k_t	Tangential elastic stiffness constants, $\mathrm{N/m}$
k_n	Normal elastic stiffness constants, $\mathrm{N/m}$
k_r	Rolling elastic stiffness constants, Nm
c	Visco-elastic damping constant, $\mathrm{kg/s}$
c_n	Normal visco-elastic damping constant, $\mathrm{kg/s}$
c_t	Tangential visco-elastic damping constant, $\mathrm{kg/s}$
δ	Overlap between particles, m
δ_t	Tangential overlap between particles, m
δ_n	Normal overlap between particles, m
s	Skin distance, m
a	Rolling resistance angle, rad
e	Restitution coefficient, -
e_{p-p}	Restitution coefficient between particles, -
e_{p-w}	Restitution coefficient between particle and wall, -
E	Young's modulus, Pa

E_{eff}	Effective Young's modulus, Pa
G	Shear modulus, Pa
G_{eff}	Effective shear modulus, Pa
I	Inertia of particle, $\mathrm{kg\,m^2}$
m	Particle mass, kg
m_{eff}	Effective mass, kg
r_{eff}	Effective radius, m
β	Dimensionless damping coefficient, -
ρ	Particle density, $\mathrm{g/cm^3}$
ρ_{bulk}	Bulk density, $\mathrm{g/cm^3}$
ν	Poisson's ratio, -
μ	Sliding friction coefficient, -
μ_{p-p}	Sliding friction coefficient between particles, -
μ_{p-w}	Sliding friction coefficient between particle and wall, -
μ_r	Rolling friction coefficient, -
$\mu_{r,p-p}$	Rolling friction coefficient between particles, -
$\mu_{r,p-w}$	Rolling friction coefficient between particle and wall, -
C_p	Mass specific heat capacity of particles, $\mathrm{J/kgK}$
C_v	Volumetric specific heat capacity of particles, $\mathrm{MJ/m^3K}$
$C_{mixture}$	Specific heat capacity of a mixture in rule of mixtures, $\mathrm{MJ/m^3K}$, $\mathrm{J/kgK}$
k	Thermal conductivity, $\mathrm{W/mK}$
k_p	Thermal conductivity of particle, $\mathrm{W/mK}$
k_{bulk}	Bulk thermal conductivity, $\mathrm{W/mK}$
k_f	Fluid thermal conductivity in ZBS model, $\mathrm{W/mK}$
α	Thermal diffusivity, $\mathrm{mm^2/s}$
P	Power in TPS theory, W

Δd	Probing depth in TPS theory, mm
r	Radius of sensor in TPS theory, mm
t	Transient measurement time in TPS theory, sec
R	Resistance of the sensor in TPS theory, Ω
R_0	Initial resistance of the sensor in TPS theory, Ω
p	Temperature coefficient of the resistivity in TPS theory, K^{-1}
ΔT_{samp}	Temperature increase in the sample in TPS theory, K
ΔT_i	Temperature difference between sensor and sample in TPS theory, K
τ	Dimensionless time in TPS theory, -
Θ	Characteristic time in TPS theory, sec
b	Thickness of insulation material in TPS theory, mm
F_τ	Function of dimensionless time in TPS theory, -
α_i	Diffusivity of insulation material in TPS theory, mm^2/s
m_{fluid}	Fluid mass in rule of mixture in rule of mixture, g
λ_{bulk}	Relative bulk thermal conductivity of the particle bed in ZBS model, $\mathrm{W/mK}$
λ_{rad}	Relative radiation coefficient in ZBS model, -
λ_c	Relative core conductivity in ZBS model, -
λ_p	Relative particle conductivity in ZBS model, -
C_f	Shape factor in ZBS model, -
φ	Flattening coefficient in ZBS model, -
γ	Accommodation coefficient in ZBS model, -
$C_{p,g}$	Specific heat of the gas in ZBS model $\mathrm{J/kgK}$
M	Molecular weight of the gas in ZBS model, $\mathrm{g/mol}$
T	Temperature of the bed in ZBS model, K
l	Modified mean free path of gas in ZBS model, m
P	Pressure in ZBS model, Pa

$f(\zeta)$	Distribution function in ZBS model, -
σ	Stefan boltzmann constant, $\mathrm{W/m^2K^4}$
ϵ	Emissivity of the particles, -
R	Universal gas constant $\mathrm{J/molK}$

CHAPTER 1

INTRODUCTION

1.1 Motivation and Problem Definition

The significant advantage of the power production systems that utilize thermal energy over the other systems is the energy storage capability at an enormous amount cheaply. Large-scale thermal energy storage (TES) can supply reliable energy according to the demand continuously without being affected by the intermittency of resources. Many different power production systems utilize thermal energy, including renewable and conventional fossil fuel systems such as petroleum, coal-fired power, nuclear power and solar thermal electricity.

Besides electricity production, thermal energy is a promising alternative to supply heat to specific industries that utilize the high-temperature process heat, such as cement production, aluminum recycling, green hydrogen production, fuel production and steel production. Some industrial processes require high-pressure steam; thermal energy systems meet this need in a cheap way. Industrial process heat comprises two-third of total industrial energy demand [1]. Studies showed that more than half of it requires high-temperature heat above 400 °C [1]. Today's industrial process heat is mostly supplied from fossil fuels nearly $\%$ 40 by natural gas and $\%$ 40 by products of petroleum [1]. With the advantage of reaching high temperatures and storing a vast amount of TES capacity, renewable thermal energy systems are good alternatives to current process heat suppliers.

One of the leading renewable power production systems operated by thermal energy is solar thermal electricity, also known as Concentrated Solar Power (CSP), which utilizes solar power's heating effect. Focused sunlight is directly used as a heat source in the CSP systems to operate thermodynamic cycles by heating working fluids. The significant advantage of the CSP systems over the other thermal energy sources and photovoltaics is the directly converting solar sources to thermal energy at an enormous amount cheaply. Also, due to the high concentration ratio of solar rays, higher temperatures can be achieved; thus, leading to more efficient thermodynamic cycles. Considering these advantages, central receiver CSP systems are getting attention and constitute a high potential for the future market. In recent years, studies on CSP systems like other power production systems have focused on reducing the levelized cost of electricity (LCOE). This reduction is possible by lowering heat losses and investment costs and by achieving higher temperatures with appropriate material selection to improve efficiency,

Heat transfer fluid, also known as the working fluid, and storage medium selection for operation is essential while designing a power plant. Both working fluid and storage media should have some specifications so that system pursues an efficient operation. High energy density, good thermal and radiative properties are required. As the state of the art, molten salts, thermal oils, air and water/steam are used as working fluid/thermal energy storage media in the energy production systems. However, the mentioned materials have several drawbacks that are discussed below:

- The maximum operating temperature for molten salt is around 600 °C and for air-liquid is about 400 °C. Low operation temperature reduces thermodynamic cycle efficiency, efficiencies of current molten salt-based systems are nearly 40 %. Low operation temperatures restrict the use of high efficient cycles such as the Bryton cycle [2].
- Most thermal oils and molten salts are relatively costly. Notably, a high amount of usage of them for the big silo storage increases the total investment cost.
- Using a two-phase air-liquid mixture, thermal oils and molten salts requires a careful operation. They could ionize and breakdown at high temperatures.
- The melting point of molten salt is around 200 °C. Molten salt should be in the liquid phase to satisfy system requirements. Thus, keeping the molten salt above 200 °C is necessary to use it as working fluid. However, this leads to additional operations and increases costs.

Solid particles are proposed as heat transfer and storage media in thermal power plants to overcome the drawbacks of mentioned materials. Solid particles are good alternatives to commercially available working fluids/storage media due to their ability to operate and to resist to higher temperatures and their low investment costs [3]. With these advantages in mind, the efficiency of the system can be increased and overall LCOE can be reduced.

In order to use solid particles inside the thermal power plants, their behavior in the system should be predicted. Macroscopically, granular media may act like fluids, but this bulk behavior is fundamentally governed by its characteristic discrete internal nature. Discrete particle behavior and interaction of particles with each other lead to the bulk response. Unlike fluid flow, continuum models cannot explain the bulk behavior of granular media. However, particle interactions explain it [4]. Moreover, particle-boundary interactions can not be described accurately by traditional continuum models, e.g., solid particles do not show no-slip boundary condition but slip at boundaries. These particle-particle and particle-boundary interactions significantly affect the heat transfer phenomena in the systems.

Solid particles to be used in thermal energy production systems as working fluid, heat absorber, and heat transfer medium should be modeled accurately before using it in real-life operations. Discrete Element Method (DEM) describes the particulate medium better than continuum models [4]. One of the significant aspects of obtaining an accurate DEM simulation is selecting the appropriate parameter set for particles. Therefore, this thesis focused on the thermal and mechanical characterization of candidate solid particle properties that are input to DEM models for modeling particles that operates in thermal energy systems.

1.2 Central Tower CSP Systems

One of the main promising fields for utilizing solid particles as heat transfer and storage media is CSP systems. According to the technology of the focus system, there are different types of CSP available in the market. Central tower receiver systems are the ones that operate at the highest temperature range above 500 °C up to 1100 °C.

Sun rays are reflected by two-axis sun-tracking mirrors to the central tower located at the middle of mirrors. These reflecting mirrors are called heliostat.

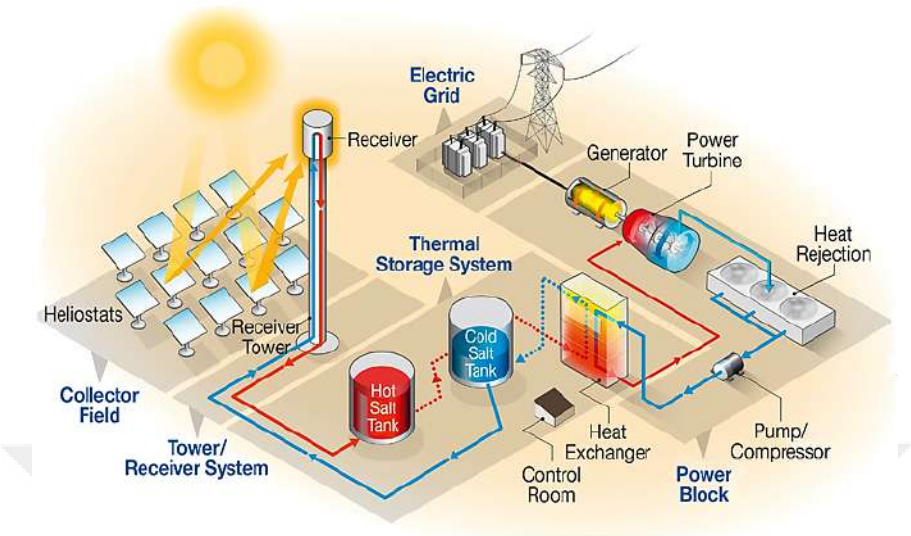

Figure 1.1: Schematics of a Concentrated Solar Power (CSP) Plant [5]

On top of the central tower, a receiver is placed to collect concentrated solar radiation. Heat transfer material in the receiver heats up due to high radiation. Depending on the heat transfer fluid characteristics, temperatures up to 1000 °C can be reached. The high-temperature material inside the receiver goes down to the ground level. At this point, one option is to store the material for later use of heat; or high-temperature material can transfer heat to the other working fluids via a heat exchanger (HEX) to run the thermodynamic cycle for energy production. Then, the cold storage material is pumped to the receiver for the next operation. The schematics and working principle of a CSP can be seen in Figure 1. Commercially available CSP systems use molten salts, liquid metals, thermal oils, air and water/steam as the heat receiver, transfer and storage medium in the system.

1.3 Particles as Heat Receiver and Transfer Media

As a novel approach, solid particles are proposed as an alternative to existing molten salts, thermal oils and heat receiver mediums to be used as direct heat transfer media [6], [7]. For example, solid particles are candidates to be used at the receiver in CSP systems as heat receiver material expose to direct or indirect irradiation and heat transfer medium as working fluid by fluidizing at heat exchangers. This idea of using solid particles in CSP systems dates back to the 1980s at Sandia National Laboratories. After some research, it ended in a couple of years. In 2004 research on solid particles re-initiated to overcome some challenges on CSPs [8].

Key challenges and requirements for the heat receiver/transfer technologies are reducing heat loss, the durability of heat absorber material at high temperatures, high absorption capacity. Solid particles outperform molten salts, thermal oils, liquid metals as a heat receiver medium. They can withstand high temperatures up to 1100 °C without any mechanical or chemical breakdown. Different novel particle receiver designs for CSP systems have been proposed by various groups around the world, such as free-falling particle receiver, centrifugal receiver, obstructed flow receiver, fluidized bed receiver and researches are going on these designs. Some particle receiver designs allow directly heating of the granular media, so this system takes advantage of reducing heat losses and getting high heat fluxes [9].

The efficiency and operating conditions of a power plant are mainly affected by heat transfer fluid. Solid particles can reach temperatures up to 1000 °C during operation. Higher the temperature of heat transfer fluid drives more efficient thermodynamic cycles [8]. The LCOE of power plants reduces dramatically with more efficient thermodynamic cycles. Also, high-temperature heat transfer fluid can run some production processes that require high-temperature process heat, such as hydrogen production [8]. Moreover, solid particles can maintain a solid phase at a wide temperature range; thus, safe operations are pursued.

1.4 Particles as Thermal Energy Storage Media

One of the significant considerations while designing a power plant is the storage system. The primary reason why particle storage systems outperform others is a high amount of TES capability. Moreover, TES provides heat recovery to the industrial processes; this contributes to the energy demand of the industry that utilizes high-temperature process heat. Desired properties of a TES system are high energy density, thermal stability to resist cycling heating, low thermal expansion and low investment cost. Storage systems account for half of the investment cost of a power plant. Molten salt storage systems, which account for more than half of the total investment cost, are very costly. In order to run a large power plant, a high amount of TES material is required. Solid particles fulfill this requirement in a cost-effective way [9]. Mainly two different TES systems available in the literature, which are packed beds and fluidized beds. Solid particles enable direct storage of heat absorber medium with fluidized beds heat exchanger system. Thus, this eliminates heat transfer from the absorber medium to the storage medium, which dramatically reduces exergy losses of the system [3].

Desirable properties of solid particles are good thermal characteristics like high heat capacity, high thermal bulk conductivity, high density, resistance to corrosion, ionization, melting, thermal shock and thermal expansion. Moreover, good radiative properties like high absorbtance and low emittance are required. Considering mentioned properties, many different particle types are examined by many researchers, including sand particles, sintered bauxite, silicon carbide, graphite pebble [10], [6], [11], [7]. One of the most popular candidate is high absorber bauxite particles that are used by many research groups [8], [12], [13], [14]. Their good radiative and thermal properties make them a good candidate to be used as both a heat absorber and a TES medium. Their chemical content composed of aluminium oxide Al_2O_3, iron (III) oxide Fe_2O_3, silicon dioxide SiO_2, titanium dioxide TiO_2, so they are not harmful for environment and human health. Natural sand particles are also considered among candidate materials because of their low or no cost and high accessibility, especially for the attractive locations that CSP systems built-in [2], [15]. Thus, sand particles and CarboHSP 40/70 bauxite particles are used to characterize in this thesis.

1.5 Modelling Particles: Discrete Element Method (DEM)

In order to design, analyze, understand the outcomes and optimize particle-based systems such as CSP particle receivers, particle TES systems, packed beds and fluidized beds, particle media should be modeled accurately. Continuum models can be insufficient while describing some typical bulk particle behavior such as particle slip boundary conditions and blockages. Since particulate media is not continuous but discrete DEM is suitable to solve typical granular phenomena like particle interactions.

DEM is a numerical method to model particulate systems. DEM was first developed in 1979 by Cundall and Strack [16]. It does not require a mesh structure. DEM uses Lagrangian approach. It applies Newton's Law of Motion to track every particle. Application of DEM in industrial processes is getting popular in particulate media dominant industries like silo discharge processes [17], bulk material handling systems [18], conveying applications [19], segregation processes [20], rotating drums [21].

As mentioned in the previous section, research of granular materials to be used as heat transfer and storage media is getting popular. However, the modeling of particles by DEM used in CSP systems is fairly novel. There are some researches on CSP systems using DEM similar approaches.

Chilamkurti et al. [22] used DEM to model gravity-driven dense granular flows as a heat transfer medium in CSP applications. Their DEM model is quite compatible with experimental findings [23]. They concluded that particle-wall contact behavior plays an essential role in that type of application [22]. DEM is also started to be used to model particle receivers. Zanino et al. [24] modeled particle curtain using DEM for falling particle receiver and showed the effect of some parameters on curtain thickness. Morris et al. [25] used DEM to validate the two-phase CFD model of laboratory-scale obstructed flow receiver. Sandlin [26] compared CFD and DEM models for obstructed particle flow used in impeded flow receivers. In this study, it is concluded that the DEM model matched with the experiment better than the CFD model, DEM predicts mass fluxes, volume fractions and particle behaviour at the boundaries more accurately than CFD for different obstructed designs [27], [28].

Also, there are some studies on DEM models in TES systems. Dreißigacker et al. [29] showed that the DEM model could predict the experimental results for particle-based thermal energy storage tanks. Sassine and Donzé et al. [30] studied thermal stresses in packed bed TES by using DEM and concluded that bed behavior depends on particle properties. Coetzee [31] modeled a packed rock bed with large rock particles by using DEM .

Understanding interactions between particles and particle and wall is essential for particle-based heat transfer and storage systems because they affect flow regimes and heat transfer phenomena in granular media. One of the primary considerations is CSP systems. Especially for some CSP components, particle interactions play a crucial role in bulk behavior, so they are design considerations. A couple of related examples are explained in the following. For obstructed flow receivers, particle-particle and particle-wall interactions affect the time that particles are exposed to irradiation or heat fluxes. Also, one of the key aspects for the design of centrifugal receiver types is residence time that particles can construct a particle layer at the receiver's wall by centrifugal force [14]. Accurate prediction of particles' bulk behavior is possible by solving particle-wall and particle-particle interactions in a precise way.

1.6 Measurement of Mechanical Properties of Particles

DEM requires a set of particle properties as input to solve particle interactions. While some properties are material properties specific to the material itself and originate from the material's nature, some properties are interaction properties that arise from particle interactions. Material properties are Young's modulus E and Poisson's ratio ν, and interaction properties are rolling and sliding friction coefficients μ_r, μ and restitution coefficient e.

One of the main challenges of DEM is to specify correct particle properties that are input to DEM. Many researchers agree that particle properties should be selected correctly to simulate the bulk behavior of the particulate systems to correspond to the real-life response. Two main approaches exist in the literature to obtain particle properties: 1) direct measurement and 2) inverse calibration method.

1.6.1 Direct Measurement Method

The direct measurement approach aims to measure particle properties directly on the particle contact level. The advantage of this method is measured particle properties do not depend on particle interaction models used on DEM. Some properties are challenging to measure at the particle level. Thus the applicability of direct measurement methods depends on the particle scale. Direct measurement of some properties is straight-forward for relatively large particles, which are at least at the millimeter level. However, for small size particles, the direct measurement method is hard to apply properly. It might require special design devices for some measurements like inter-particle friction coefficients.

Many researchers used different direct measurement tests for different properties. Chen et al. [32] performed inclined plane test for 10 mm glass beds. Barios et al. [33] used a rotating pin on disk tribometer to measure the sliding friction coefficient between wall and particle for 12.5 mm iron core particles. Some researchers used drop test to measure the restitution coefficient between particle and wall for particles whose sizes are in cm level particles [33], [34]. Li et al. [35] directly measured Young's Modulus of 2-10 mm iron core particles by direct compression test.

Direct measurement of properties for small-scale particles is a challenging process. Some researchers developed special design test setups for that purpose. Senetakis et al. [36] developed shear test apparatus to measure inter-particle friction. This apparatus applies a tangential force on a particle via the other particle on top of it. That tangential force can displace in a range of 1 $\mu\mathrm{m}$- 300 $\mu\mathrm{m}$ displacements. Sandeep et al. [37] measured sliding friction coefficients between quartz sand particles by using the same test setup. Many researchers performed direct measurement of particle-wall sliding friction coefficients for small particles by using shear boxes which is a device that applies shear force on particles via flat wall material [38], [39].

1.6.2 Inverse Calibration Method

Direct measurement of some properties can be difficult, especially for small-size particles. In reality, all particles do not have the same shape and sizes. Interaction properties between particle pairs of different shapes and sizes will not be the same. Thus, all particles cannot have the same material properties and it is not possible to measure properties for all particles.

The calibration method makes use of bulk level tests. DEM simulations of a real-life bulk test are performed with many different parameters iteratively. The important point is that the concerned parameters should be changed individually by keeping the others constant. The aim is to find the correct parameter set that bulk behavior matches the real-life result. Numerous bulk tests were developed for calibration approach; some examples are static Angle of Repose (AOR), bulk shear test, rotating drum (dynamic AOR) test, bulk compression test. Also, some researchers developed different test setups for different bulk behavior experiments. However, as a significant disadvantage of this method, bulk behavior might be affected by more than one property. This leads that many parameter sets give the same bulk behavior result [40].

AOR is a widely used bulk test in the literature with its various versions. Marigo et al. [21] calibrated all interaction properties by using AOR. However, they did not change parameters individually by keeping the others constant. They inputted guessed parameter sets, and they choose the most appropriate parameter set that fits the experiment, among the guessed ones. Combarros et al. [20] calibrated inter-particle friction coefficients by the static and dynamic angle of repose, but they did not consider wall friction coefficients. Derakhshani et al. [41] performed AOR and discharge time test to calibrate inter-particle friction coefficients . However, they did not perform any sensitivity tests. Roessler et al. [42] performed detailed calibration for particle-particle friction coefficients using AOR, discharge time and mass flow rate. They obtained a unique parameter set, but they do not validate the obtained parameters. The bulk shear test is another option for calibration of rolling and sliding friction coefficients, but one should consider that it requires an additional bulk test for robust calibration [40].

1.7 Investigation of Thermal Properties in the Literature

As mentioned previously, using solid particles as heat transfer and storage media is a relatively new concept. The thermal properties of the particulate medium are one of the important aspects to evaluate the feasibility of systems integrated with particle heat transfer/storage media. Particles are in a thermal cycle between 300-1000 °C in related systems such as thermal power plants. The efficiency of a system depends on the amount of heat absorption in the heat transfer medium, thermal energy storage capacity in the TES system, amount of heat transferred while discharging the storage to run the power cycle. Also, thermal losses from the system are important factors that affect efficiency. Thus, the thermal behavior of the bulk granular medium comes into question.

Since particles are used as the heat transfer and storage medium in power plants, high heat capacity is required for more efficient power production. To calculate storage capacity and lifetime, specific heat capacity and conductivity of particles involve in computations. Baumann et al. [10] stated that conductivity is crucial for particle-based HEX design to determine thermal charging and discharging of the bulk medium. Moreover, heat capacity is one of the critical parameters for receiver designs.

Thermal properties of particles are input to heat transfer models of particulate materials. Thus, the bulk thermal behavior of the granular medium can be predicted. Also, while modeling coupled medium with particle fluid interactions, fluid and particle properties should be specified separately. Accurate temperature-dependent data for particles' thermal properties is necessary for accurate models and efficient computations on CSP systems.

Some granular materials are proposed as candidates by many research groups; popular ones are sintered bauxite particles and naturally available sand. Sintered bauxite particles are engineered materials for different industries, such as the fracturing industry for mining, but not produced explicitly for thermal energy applications. Nevertheless, since their good radiative properties and resistivity to high temperatures, they are proposed to be used as a heat transfer and storage medium. Sand particles are cheaply available in nature; they are economical alternatives as a heat transfer medium since a vast amount of particles are needed. Thermal properties of bauxite particles are not supplied by the manufacturer. Also, sand's chemical composition can differ depending on its location; this affects its thermal properties. Specific heat capacity and conductivity of the granular media should be known to select the best material for optimum operating conditions.

The measurement of the thermal properties of the particles is a challenging task. Since they are in the range of $\mu\mathrm{m}$ to mm, it is not possible to measure particles' thermal properties at the particle level. Measurement of granular materials' thermal properties as bulk is a difficult process because of their discrete nature. There are many different thermal property measurement methods based on different principles. In order to measure thermal conductivity, steady-state and transient methods are available such as guarded hot plate as steady-state method; hot wire, hot strip and hot disk as the transient methods. Moreover, different types of Differential Scanning Calorimeter (DSC) are commonly used to measure specific heat capacity.

There are not much available data in the literature for the thermal properties of particles used as heat transfer and storage medium. Baumann and Zunft [10] measured the effective conductivity of sintered bauxite and sand particles by using the hot-wire method and specific heat by DSC. However, they did not specify the sintered bauxite particles that they measured. The only available data of specific heat capacity for the CarboHSP particles is supplied by Siegel et al. [12].

1.8 Thesis Overview

1.8.1 Proposed Method, Contributions and Novelties

Novel particle-based heat transfer and storage systems and their components are just started to be modeled by DEM to predict system behavior accurately [23], [22], [24], [25], [26], [27], [28], [29], [30], [31]. To accurately model the particle system, particle properties should be inputted into the DEM properly. In this thesis, the DEM mechanical and thermal properties of particles that are candidates to be used as heat transfer and storage media are investigated. Most popular candidate materials sintered bauxite CarboHSP 40/70 and sand particles were chosen to be examined. Direct measurement and calibration approaches were used together to obtain an accurate set of DEM mechanical properties. DEM models of real-life discharge tests were repeated with many parameters set to meet real-life response and obtain the exact parameters for the calibration part. LIGGGHTS [43] open-source DEM software was used in this thesis to compute forces acting on particles and numerical integration of motions. LIGGGHTS is developed from molecular dynamics software LAMMPS. Since it is open-source software, different motion integrations and contact interaction models can be implemented. Also, it can be coupled with CFD for two-phase problems.

Particles operate at high temperatures as heat transfer and storage medium. Thus, bulk measurement tests were repeated with high-temperature particles to see particles' behavior at high temperatures and investigate any difference in particle properties. In addition to high-temperature particles, thermally cycled particles were tested. In closed-loop cycles like in CSP systems, particles are heated to high temperatures and cooled down. To meet thermal cycling in real systems, particles were thermally cycled by heating up in a furnace and then were cooled to room temperature.

Moreover, the thermal properties of particles were measured by the Transient Plane Source (TPS) method hot disk measurement device. As mentioned in the previous section, there is only one available data in the literature for CarboHSP particles' specific heat capacity. Specific heat measurement was performed by the TPS method Hot disk device to verify this data. Bulk thermal conductivity k_{bulk} of particles as a function of temperature is measured. Results are compared with the Zehner-Bauer-Schlünder (ZBS) model [44].

1.8.2 The Outline of the Thesis

The content of this thesis is separated into two parts: 1) investigation of DEM mechanical properties; and 2) the investigation of thermal properties. Firstly, to obtain DEM mechanical properties, direct measurement and inverse calibration method using DEM analysis were used together. Calibration tests were repeated both at high temperatures and with thermally cycled particles to figure out if particle properties changed at high operating temperatures and after thermal cycling. The second part is the measurement of thermal properties. To validate old available measurement data in the literature, the temperature-dependent thermal properties of the particles were measured by TPS hot disk device at high temperatures. The outline of the thesis is as follows;

Particle-based heat transfer and storage media are introduced and its advantages over the state of the art molten salt systems are mentioned in Chapter 1. The modeling method for the particulate system and requirements are explained. Why the investigation of particle input properties for this thesis motivates the author is discussed.

Fundamentals of DEM and input particle properties are expressed comprehensively in Chapter 2.

DEM mechanical properties of particles are investigated in Chapter 3 by utilizing direct measurement and the inverse calibration method.

Particles' durability under thermal cycling and at high temperatures are examined in Chapter 4.

Thermal properties of candidate particles are investigated by utilizing the Hot Disk equipment and only available literature data for CarboHSP particles are verified in Chapter 5.

The overall study is concluded and future work with investigated particle properties is mentioned in Chapter 6.

CHAPTER 2

FUNDAMENTALS OF DISCRETE ELEMENT METHOD

2.1 Equations of Motions and DEM Numerical Computation

In this part, the computational mechanism of the Discrete Element Method (DEM) is discussed. As mentioned before, DEM applies the Lagrangian method, which leads every motion equation is solved for each particle individually.

Net force and moment acting on an individual particle [45]:

$$F_{net} = m\frac{dV}{dt} = F_{particle-particle} + F_{external} + F_{fluid-particle} \tag{2.1}$$

$$M_{net} = I\frac{d\omega}{dt} = M_t + M_r \tag{2.2}$$

$$M_t = F_{tangential} \times r \tag{2.3}$$

V and ω are linear and angular velocities of particles, I is the inertia and m is the mass of a particle.

External force $F_{external}$ can be any exterior force like the gravitational force, the magnetic force on a magnetic environment. Only the gravitational force is taken into account in this study as an external force. Interaction between fluid and particle is created by fluid-particle forces $F_{fluid-particle}$, and it can be explained by the two-phase coupled CFD-DEM model. Any dominant fluid interaction does not exist in this study, so fluid interaction forces are neglected in the motion equations. Interaction forces between two particles $F_{particle-particle}$ are explained by force contact models between particles. M_t is the total moment created by tangential forces acting on a particle. Since fluid interactions were not included in this study, particle-particle tangential interaction forces are the only forces that create the tangential moment. M_r is the rolling resistance moment that acts opposite to rotation and it will be discussed in detail in the related chapter. Forces and moments acting on particles and velocities created by these forces are shown in detail in Figure 2.1.

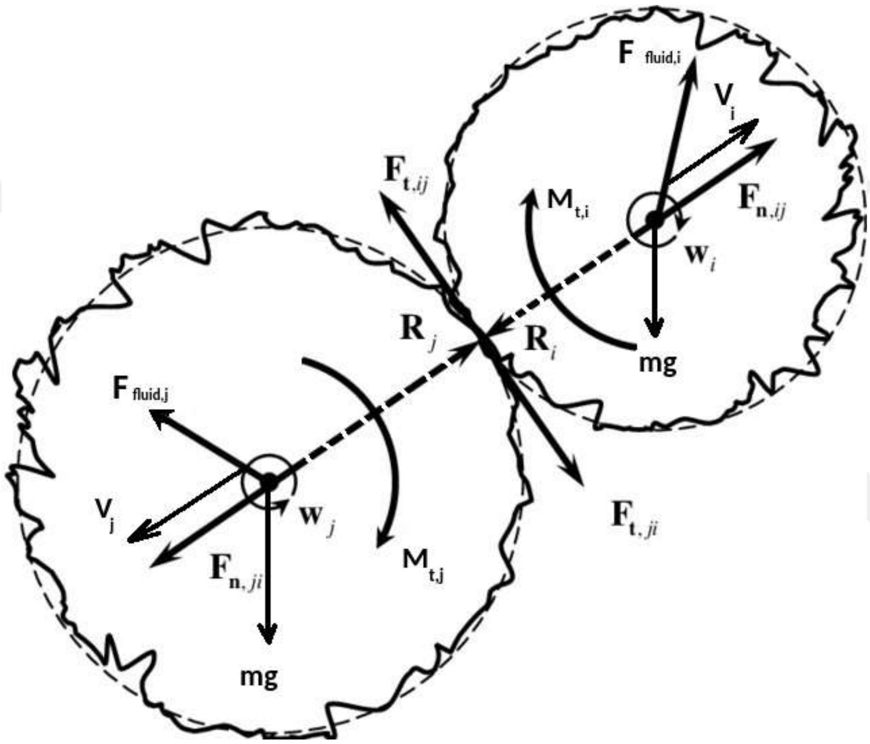

Figure 2.1: Interaction forces acting on particles

To be computationally effective, DEM does not check every other particle to find which ones are in contact with a specific particle. However, it uses a contact detection algorithm to figure out which particles are in touch during the simulation. The idea is to keep the possible contacts for a particle in a list called the neighbor list. A pair of particles added to the neighbor list if they satisfied the criteria,

$$|x_i - x_j| \leq R_i + R_j + s \tag{2.4}$$

x_i and x_j are particle positions of particle i and j at a specific time step. R_i and R_j are particles' radius and s is the so-called skin distance.

This neighbor list is valid for Velocity verlet time step N_{verlet} [43]:

$$N_{verlet} = \frac{s}{V_{max}\Delta t} \tag{2.5}$$

Δt is the constant time step and V_{max} is the maximum particle velocity at that time step.

If one sets the skin parameter to a high value, it is required to check many neighbor particles in a neighbor list, but it is not necessary to build a new list often. The other way around, setting the skin diameter small reduces possible checks for candidate neighbor particles, but the neighbor list should be updated more frequently. In this thesis, the skin parameter was set to one particle diameter and neighbor lists were built at every time step.

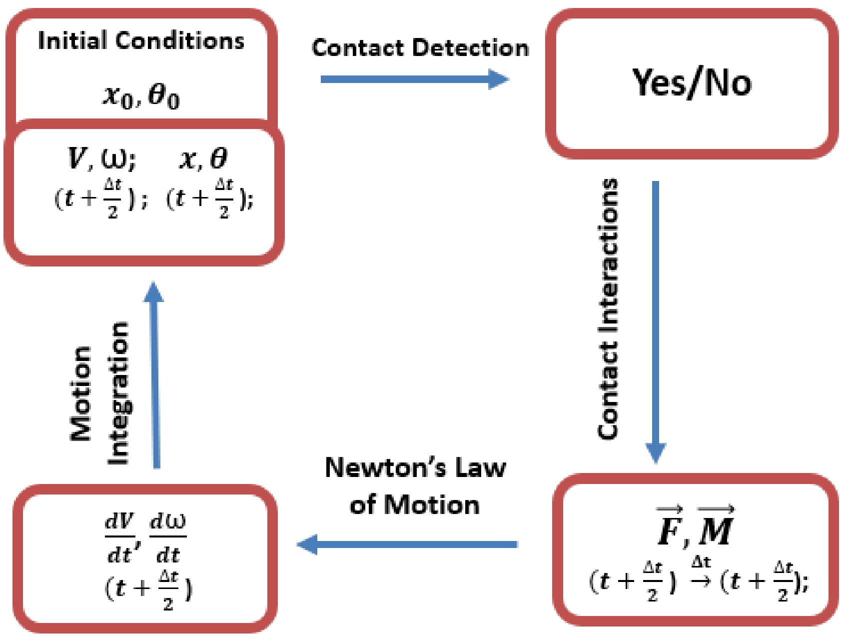

Figure 2.2: Numerical computational flowchart of DEM calculations

As explained in Figure 2.2, DEM takes initial positions and velocities of particles as input and then applies the contact detection algorithm to find possible particle interactions. As a result of the interaction forces that affect particles, new linear and angular accelerations are calculated by using Newton's law of motion particles. By motion integration, new velocities and positions are calculated for each particle [46].

2.2 Contact Models and Interactions between Particles

There are many available contact models in LIGGGHTS to model particle interactions. Accurate modeling of collisions is essential to obtain actual resulting forces. One way to predict proper particle collisions in DEM is to model particles as soft spheres. One can see in Figure 2.3; as a result of an elastic collision, overlaps occur between particles. Nonlinear visco-elastic model Hertz models the contact forces during the collision as springs and dashpots that are functions of overlap.

The first part of the Hertz contact model, which is composed of spring and damping forces, predicts the normal force component; the second part, which is composed of shear and damping force, indicates the tangential force component. Thus total interaction forces are formulated as;

$$F = (k_n \delta_{n_{ij}} - c_n V_{n_{ij}}) + (k_t \delta_{t_{ij}} - c_t V_{t_{ij}}) \tag{2.6}$$

where $\delta_{n_{ij}}$ is normal overlap between particles, $\delta_{t_{ij}}$ is tangential overlap between particles, k_n is elastic stiffness constant in normal direction contact, k_t is elastic stiffness constant in tangential direction contact, $c_n \geq 0$ is visco-elastic damping constant for normal direction, $c_t \geq 0$ is visco-elastic damping constant for tangential direction, $V_{n_{ij}}$ is relative velocity between particles in the normal direction, $V_{t_{ij}}$ is relative velocity between particles in the tangential direction.

Elastic stiffness constants k_n, k_t, and visco-elastic damping constants c_n, c_t are depend on particle properties Young's modulus E, Poisson's ratio ν and restitution coefficient e. Derivations of them from material properties of particles can be seen in the following formulations.

Elastic stiffness constant k in normal and tangential directions:

$$k_n = \frac{4}{3} E_{eff} \sqrt{R_{eff} \delta_n} \qquad k_t = 8 G_{eff} \sqrt{R_{eff} \delta_n} \tag{2.7}$$

Visco-elastic damping constant c in normal and tangential directions:

$$c_n = -2 \sqrt{\frac{5}{6}} \beta \sqrt{S_n m_{eff}} \qquad c_t = -2 \sqrt{\frac{5}{5}} \beta \sqrt{S_t m_{eff}} \tag{2.8}$$

$$S_n = -2 E_{eff} \sqrt{R_{eff} \delta_n} \qquad S_t = 8 G_{eff} \sqrt{R_{eff} \delta_n} \tag{2.9}$$

β is the dimensionless damping coefficient:

$$\beta = \frac{\ln{(e)}}{\sqrt{\ln^2{(e)} + \pi^2}} \tag{2.10}$$

Effective Young's modulus E_{eff} is defined as:

$$\frac{1}{E_{eff}} = \frac{1 - {\nu_i}^2}{E_i} + \frac{1 - {\nu_j}^2}{E_j} \tag{2.11}$$

Effective shear modulus G_{eff} is defined as:

$$\frac{1}{G_{eff}} = \frac{2(2 - \nu_i)(1 + \nu_i)}{E_i} + \frac{2(2 - \nu_j)(1 + \nu_j)}{E_j} \tag{2.12}$$

Effective radius R_{eff} is defined as:

$$\frac{1}{R_{eff}} = \frac{1}{R_i} + \frac{1}{R_j} \tag{2.13}$$

Effective mass m_{eff} is defined as,

$$\frac{1}{m_{eff}} = \frac{1}{m_i} + \frac{1}{m_j} \tag{2.14}$$

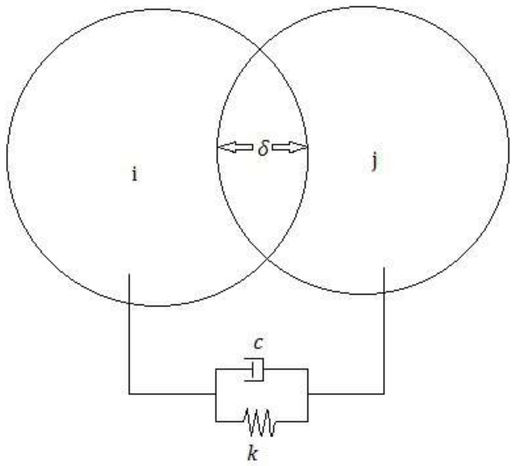

Figure 2.3: Interaction between two particles in contact in normal direction

Tangential overlap is taken into account with the history effect, so the tangential history model is added to Hertz. Coulomb's friction criterion limits the magnitude of the tangential force that two particles started to slide on each other. Columb's friction is a representation of shear interaction between two particles with the introduction of sliding friction coefficient μ.

$$F_t \leq \mu F_n \tag{2.15}$$

According to the spring-dashpot model, tangential force grows until $F_t = \mu F_n$ then it is held at this point until particles lose contact. That means the damping coefficient only exists when particles are in touch but not sliding on each other. Columb's friction is active when particles slide on each other. The coefficient of friction μ is represented as below:

$$\mu = F_t/F_n \tag{2.16}$$

The mentioned model and all formulations are also valid for particle-wall interactions by considering the walls as particles with infinite radius and mass.

2.3 Rolling Friction Model and Particle Shape Compensation

Particle collisions have a rotational component as an addition to normal and tangential components. As mentioned in Section 2.1 contribution of the total moment acting on a particle is the rolling resistance moment.

Ai et al. reviewed four different rolling models [47]. Model C in their study predicts rolling behavior more realistically compared to others. LIGGGHTS uses a modified version of Model C called Elastic-Plastic Spring Dashpot 2 (EPDS2). Although it is named as dashpot, there is no dashpot in the LIGGGHTS version of the model.

$$M_r = M_k + M_d \tag{2.17}$$

M_k is the spring moment and M_d is the spring damping moment. In the modified version of model C in LIGGGHTS, damping moment is disabled.

$$M_r = M_k \tag{2.18}$$

$$M_k = -k_r \Delta\theta \tag{2.19}$$

$\Delta\theta$ is incremental relative rotation between two particles. Rolling stiffness constant k_r is defined as

$$k_r = k_t R^2 \tag{2.20}$$

The spring moment is limited by the full mobilization moment M_m.

$$M_k \leq M_m \tag{2.21}$$

M_m is controlled by the coefficient of rolling friction μ_r and also the normal force F_n

$$M_m = \mu_r R F_n \tag{2.22}$$

The coefficient of rolling resistance μ_r is defined by Ai. et al. as [47],

$$\mu_r = \tan a \tag{2.23}$$

a is the rolling resistance angle, which is the maximum slope angle that moment produced by rolling resistance counterbalances the moment produced by the particle's weight at the contact point.

It is obvious that particles, in reality, have no perfect sphere shape. LIGGGHTS can model different particle shapes like superquadrics, ellipsoid, convex hull. One of the common methods to model irregular shape particles is to model them as a composition of many overlapping spheres. However, these particle shape models are computationally time-consuming and they are under development.

The best practice to model the sand and CarboHSP 40/70 particles tested in this thesis is to model them as pure spheres. By adding the rolling friction model, real shape behavior is compensated.

2.4 DEM Time Step and Young's modulus Reduction

DEM requires sufficiently small time step for accurate results. All of the forces acting on a particle should be detected while particles travel short distances until the next collision. There are two important criteria that restrict the DEM time step to catch all of the collisions.

Rayleigh time step Δt_r is explained as;

$$\Delta t_r = \frac{\pi r \sqrt{\rho_p / G}}{0.1631\nu + 0.8766} \tag{2.24}$$

ρ_p is density of the particle and shear modulus is explained as; $G = E/2(1+\nu)$.

Hertz time step Δt_h is explained as;

$$\Delta t_h = 2.87 \times (\frac{m_{eff}^2}{r \times E_{eff}^2 \times V_{max}})^{0.2} \tag{2.25}$$

where V_{max} is the maximum velocity exist in the simulation at that time step.

The Rayleigh criteria is a measure of force propagation distance. This distance should not be larger than the particle diameter that force is acting on. Hertz time is required to ensure that when two particles are in contact and all of the forces are mapped.

Rayleigh and Hertz times are calculated periodically during the simulation. Common idea in the literature, it is better not to exceed 20 $\%$ of Rayleigh time step Δt_r and 10 $\%$ of Hertz time step Δt_h [48], [41], [49], [50]. These fractions are implemented on the LIGGGHTS code. DEM time step does not exceed these values for simulations performed in this thesis.

On the other hand, small time steps cause very long computational time and restrict the efficiency of DEM simulations. One can notice that the time step strongly depends on particle properties. It is inversely proportional to the squarer root of G. Reduction of Young's modulus E is common practice to speed up DEM simulations [49], [50], [26]. Further studies showed that the reduction of E has no effect on AOR and discharge time/mass flow rate [51], [52].

2.5 Particle Properties

DEM requires particles' and their interaction properties as input to obtain true contact interactions between particles and solve equations of motions and then track particle velocities and positions at each time step. Required particle properties input to DEM for Hertz Midlin and EPSD2 model are Young's modulus E, Poisson's ratio ν, sliding friction coefficient μ, rolling friction coefficient μ_r and coefficient of restitution e.

E and ν are material properties. They keep their standard definition for materials when one mentions particles. Friction coefficients μ, μ_r and coefficient of restitution

e are interaction properties. They appear when particles are in contact.

The coefficient of restitution e is a measure of collision elasticity.Value of e should be between 0 and 1. $e = 0$ represents perfectly inelastic while $e = 1$ represents perfectly elastic collision. $0 < e < 1$ shows real-world inelastic collision that some energy dissipated during a collision.

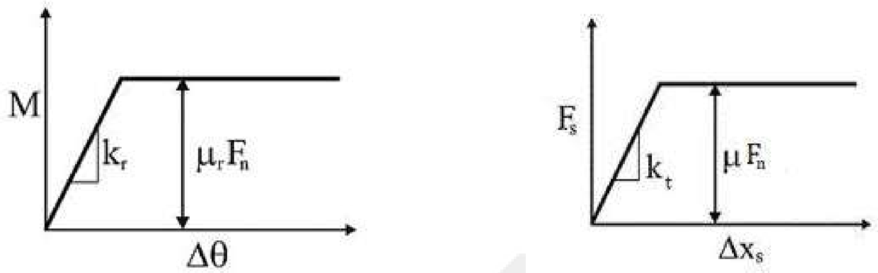

(a) Rolling Friction Mechanism (b) Sliding Friction Mechanism

Figure 2.4: Rolling and sliding friction resistances vs angular and linear displacements

Sliding friction coefficient μ is defined as the ratio of force that exceeds the friction force to the normal force component (Figure 2.4 (b)) [53]. That is the resistance of the two body sliding on each other.

Rolling friction coefficient μ_r is defined as the ratio of the moment required to start rolling by exceeding the rolling friction force to moment produced by the weight of the particle at the contact point (Figure 2.4 (a)) [53]. In other words, it is the resistance of two bodies rolling on each other.

Different from material properties, interaction properties are input to DEM as a symmetric matrix. For each DEM simulation performed, two material types are defined, one for particles and one for walls. So interaction properties exist between two particles and particles and walls. As mentioned before, walls are described as particles with infinite radius and mass; and interaction properties are applied accordingly.

CHAPTER 3

INVESTIGATION OF MECHANICAL PROPERTIES

3.1 Particle Size and Density

3.1.1 Particle Size

Figure 3.1: Tested particles: CarboHSP 40/70 (left) and sand (right)

Sand particles and sintered bauxite CarboHSP 40/70 particles are tested in this thesis (Figure 3.1). Particle properties might differ according to their sizes. Particle size analysis was performed by METU Central Laboratory. Malvern Mastersizer 2000 equipment was used, which measures the particle size with the laser diffraction method. Particle size analysis results can be seen in Figures 3.2 and 3.3.

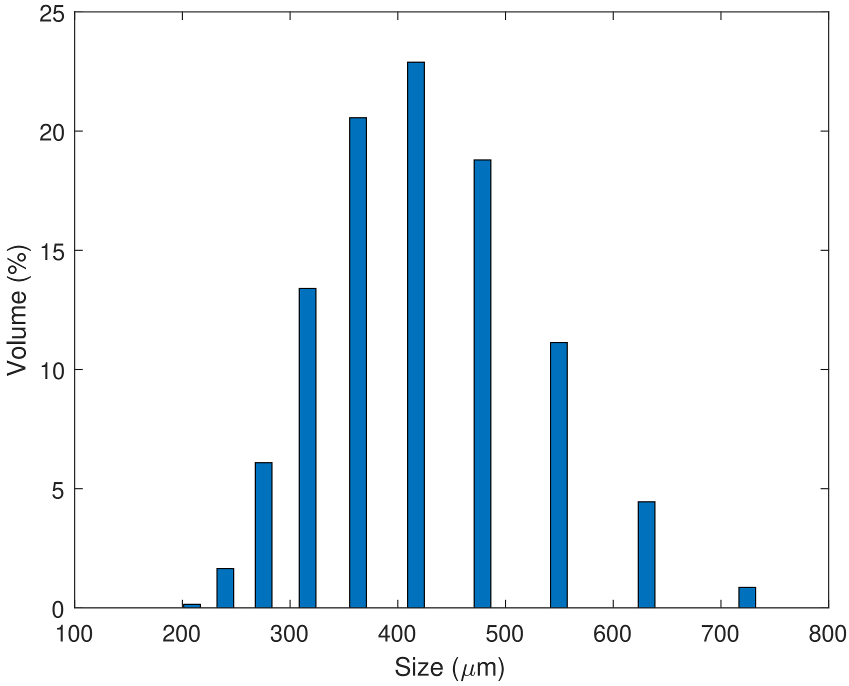

Figure 3.2: Size distribution of CarboHSP 40/70 particles

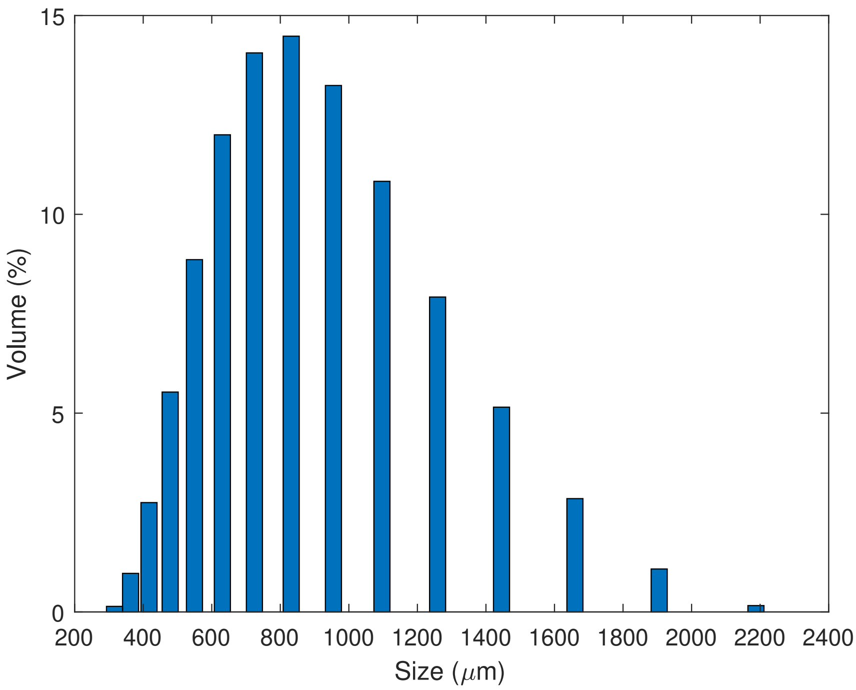

Figure 3.3: Size distribution of sand particles

3.1.2 Particle Density

Measuring the density of the particles ρ_p is a challenging process. Bulk density ρ_{bulk} and particle density ρ_p differ from each other. ρ_{bulk} is always lower than the ρ_p because of the granular nature of particles. The water submerged method was applied for ρ_p measurement is explained as follows. Particles are weighed by a sensitive scale. Then the known weight of bulk particles is added to a known volume of water. The change of volume gives the actual volume of the particles. The test was repeated 10-12 times with the different weights of particles and different volumes of water. To reduce measurement errors sensitive scale and volume measurement cylinder with 1 ml graduation were used. ρ_p of carbo particles is given by the manufacturer as 3.560 $\pm$ 0.07 $\mathrm{g/cm^3}$, which is close to the measured value of this thesis (Table 3.1).

Table 3.1: Bulk and particle density of sand and CarboHSP 40/70 particles

	CarboHSP 40/70	**Sand**
Particle Density ρ $(\mathrm{g/cm^3})$	3.592 $\pm$ 0.021	2.523 $\pm$ 0.029
Bulk Density ρ_{bulk} $(\mathrm{g/cm^3})$	2.115 $\pm$ 0.032	1.526 $\pm$ 0.035

3.2 Direct Measurement of Particle-Wall Friction Coefficients

The inclined plane test is performed for both measurements of rolling and sliding friction between particles. The particles are placed on a flat surface, and then it is given an inclination gradually to the surface. At a specific angle, the tangential component of the particle weight overcomes the frictional force; the particle starts to roll or slide down. As stated in Equations 2.16 and 2.23, the tangent of the mentioned angle is equal to the sliding friction coefficient between particle and wall μ_{p-w} if particles slide-down or equal to the rolling friction coefficient $\mu_{r,p-w}$ if particles roll-down. However, as stated in the literature (reviewed in Section 1.6.1), inclined plane tests are mostly performed for relatively big particles (particle size > $1\mathrm{mm}$).

Firstly, particle-wall friction measurements were performed by putting particles on a flat metal surface and giving inclination to the surface. However, bauxite particles and small sand particles did not just roll or slide; they bounced on the surface. This bounce is maybe because they do not have a perfect sphere shape or maybe because the flat plane's surface is not perfectly smooth to roll or slide down for that kind of small particles.

Rolling or sliding friction coefficients that particles demonstrate on a surface and the friction coefficients that surface demonstrate on particles are the same. Thus, DEM analysis software LIGGGHTS keeps the friction coefficients as a symmetric matrix :

$$\mu, \mu_r = \begin{bmatrix} p-p & p-w \\ w-p & w-w \end{bmatrix} \tag{3.1}$$

Particle-wall and wall-particle friction coefficients should be the same to satisfy the symmetricity of the matrix. Since walls do not touch each other in the applications of this thesis, wall-wall friction coefficients are not relevant.

Considering the symmetric friction coefficient matrix, instead of measuring the friction coefficients that particles demonstrate on the wall, friction coefficients that the wall implements on the particles were measured. Measurements were performed by sliding a flat metal surface and by rolling a metal ball on a flat surface covered by particles. As one can see from Figure 3.4, particles were glued on a flat surface. Metal surfaces and metal balls were used to measure rolling and sliding friction coefficients. The measurement test setup can be seen in Figure 3.5.

(a) CarboHSP 40/70 (b) Sand

Figure 3.4: Glued particles on flat surfaces

Figure 3.5: Inclined plate test setup

3.2.1 Wall-Particle Rolling Friction Measurement

Different size metal balls were placed on a flat surface on which particles glued on it. The plate was started to inclined slowly from one side by keeping the other side is fixed. Angles that balls started to roll-down was recorded. Tangent of this angle is equal to rolling friction coefficient between particle and wall $\mu_{r,p-w}$. Sizes of metal balls that were tested are 28 mm, 22 mm, 18 mm, 11 mm, 9 mm, 8.8 mm, weights are 80 gr, 43.5 gr, 25 gr, 6 gr, 3 gr, 3 gr. 12-15 measurements were taken for each ball.

The 28 mm, 22 mm, 18 mm, and 11 mm size balls perfectly rolled-down more or less at same angles on CarboHSP 40/70 particles covered surface; however, 9 mm and 8.8 mm balls became stuck between particles. On sand particles, only 28 mm and 22 mm balls rolled without sticking. This shows that the metal ball's size and weight do not affect the angle at which the metal ball starts to roll. However, the critical point is using big enough balls in size and weight to prevent the ball from stuck between particles. Big enough balls compared to one particle size compensate infinity radius and mass. If balls are not big enough, they are stuck between particles. Moreover, to examine the test's reliability, metal balls were placed on different locations on the surface. It was observed that the location of balls does not affect the inclination angle.

Table 3.2 shows the mean values of tests performed by different sizes of balls and the standard error of the mean of the test. Standard deviations are minimal, so it shows that the rolling friction test is repeatable.

Table 3.2: Measured rolling friction coefficients between metal wall and particles

	CarboHSP 40/70	**Sand**
$\mu_{r,p-w}$	0.12757 $\pm$ 0.005	0.15974 $\pm$0.011

3.2.2 Wall-Particle Sliding Friction Measurement

The inclined plane test was repeated to investigate sliding friction coefficients μ_{p-w} between particles and the wall. A metal plate was placed on a surface on which particles glued on it. The plate was started to incline gradually. Then, the angle that the metal surface began to slide down was recorded. The tangent of that angle is equal to the μ_{p-w}. Tests were repeated 12-15 times and results are shown in Tables 3.3 and 3.4

As seen in Figure 3.6, different sizes and shapes of metal plates were tested. The 100 cm^2 metal plates that has different shapes, and square metal plates with different areas (25 cm^2 and 400 cm^2) were used. It is shown that the shape and area of plates do not affect sliding friction coefficients. Also, tests were repeated by placing plates at different locations of the particle glued surface. It is observed that the plates' location does not have any effect on the sliding friction coefficient μ_{p-w}.

A glass surface was also tested to show that different material surfaces slide at different inclination angles. Results are shown in Tables 3.3 and 3.4. As expected μ_{p-w} of the glass wall is less than the μ_{p-w} of the metal wall and for both materials. Measurement deviations are small. Thus, it can be said that this test is reliable and repeatable.

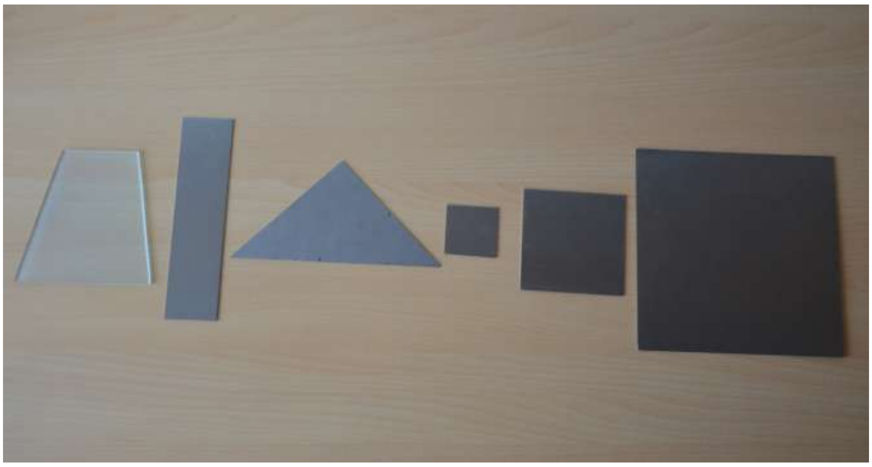

Figure 3.6: Metal surfaces used for wall sliding friction coefficient measurements

Table 3.3: Measured sliding friction coefficients between metal wall and particles

	CarboHSP 40/70	**Sand**
μ_{p-w}	0.43314 ± 0.0044	0.39619 ± 0.0057

Table 3.4: Measured sliding friction coefficients between glass wall and particles

	CarboHSP 40/70	**Sand**
μ_{p-w}	0.23938 ± 0.01232	0.24785 ± 0.0184

One can notice from Tables 3.2 and 3.3 particle-wall friction coefficient values between the metal surface and particles do not change according to the particle type significantly. μ_{p-w} values between the metal wall and particles are nearly the same for sand and CarboHSP 40/70. The same case is valid for $\mu_{r,p-w}$. The reason for it can be attributed to the same metal wall surface. Supporting this claim is that μ_{p-w} between particles and the glass surface is different from that between the metal surface and μ_{p-w} is nearly identical for between particle types and the glass surface.

3.3 Calibration of Particle-Particle Friction Coefficients

Particle-wall friction coefficients were obtained in previous sections. As stated in Section 1.6.1, direct measurement of inter-particle friction coefficients for small particles is difficult. Thus, the calibration approach was utilized for the investigation of inter-particle friction coefficients.

While applying the calibration method, one should be careful because, as stated before, more than one parameter can affect the bulk response. To overcome this problem, two bulk measurements, which are the outcomes of one bulk test, were performed. The discharge test was utilized, discharged mass amount and static AOR were measured. Then on DEM, the discharge test was repeated with different parameter sets. The parameter set that fulfills both discharged mass and AOR is the exact particle-particle sliding and rolling friction coefficients.

3.3.1 Hands on Tests

A metal funnel with an orifice at the end was used. Figure 3.7 shows the test setup. Particles were poured from the orifice; some particles stay in the funnel above the orifice by holding each other by the effect of sliding and rolling friction forces between them. Particles that are poured formed a particle pile on a metal surface that is 4 cm below the orifice. The base angle of that pile gives the Angle of Repose (AOR). The primary reason that the particle pile occurs is friction forces between particles. So, AOR is a widely used calibration test for the investigation of inter-particle friction coefficients. Discharged mass measurement was chosen as a second bulk test since friction coefficients play a significant role in it.

The same funnel was used for both sand and CarboHSP 40/70 particles. For different particle sizes, orifice size should be adjusted accordingly to obtain frictional flow. Orifice diameter should be large enough to let particles flow down and small enough to see the evident difference on discharged mass with different frictional parameter sets.

Moreover, DEM computational time depends on the particle amount and total test time. Since many different parameter sets are checked, calibration is computationally costly, especially for small particles. In addition, long-running tests with smaller orifices extend the simulation time. Considering these factors, the particle amount that is tested was kept little for ease of computation. Each measurement was repeated at least 10 times. Table 3.5 shows the total tested mass and used orifice diameter for each particle type and real-life measurement results. Test number of AOR measurement for sand particles was increased enough to solve the problem of ambiguous parameter combinations in the calibration and accurately obtain friction coefficients. It can be seen from Table 3.5 that the AOR deviation of sand is small.

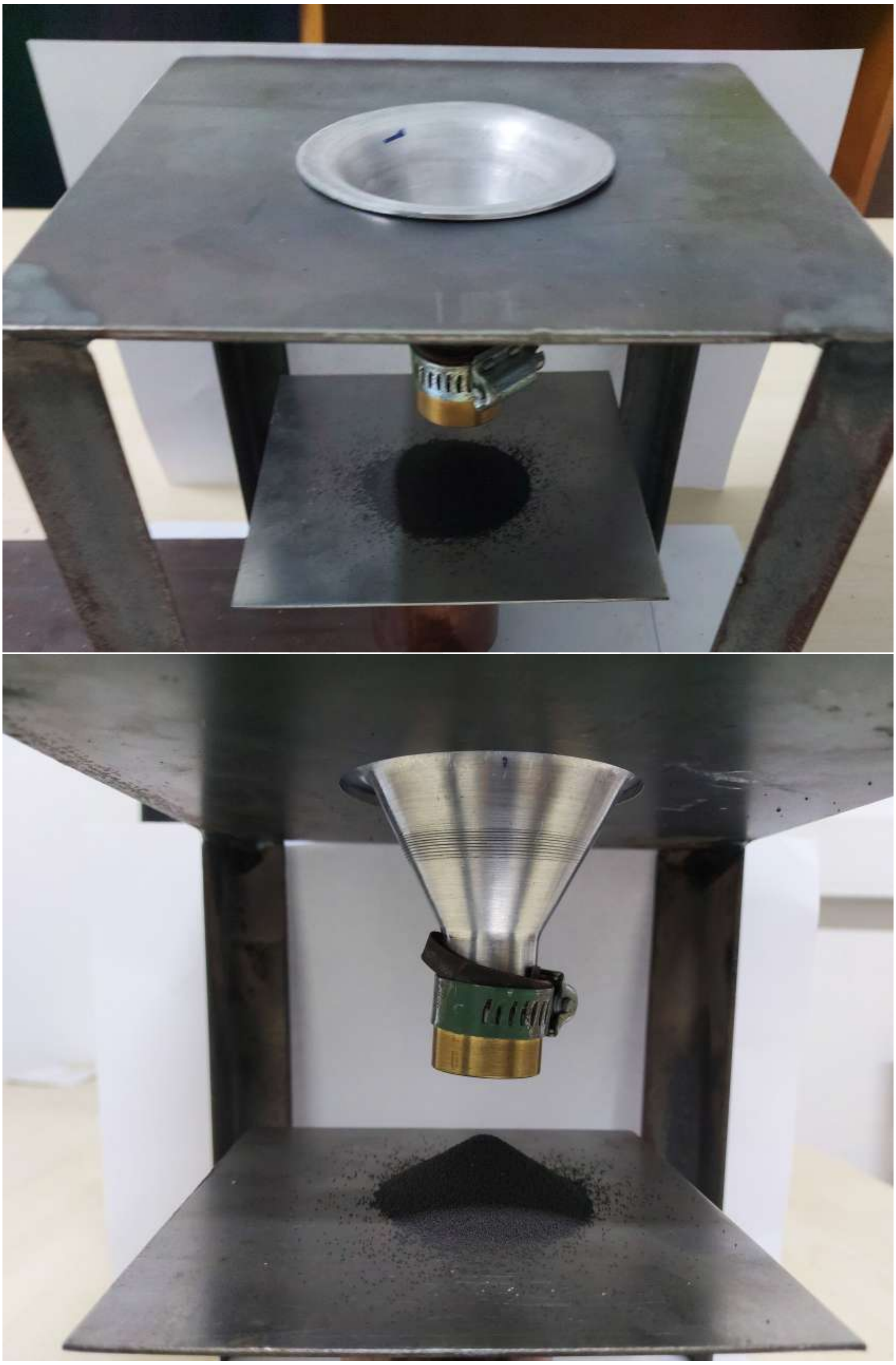

Figure 3.7: Discharge test setup: funnel, metal plate and particle pile: top view (top) side view (bottom)

Table 3.5: AOR and discharged mass measurements for sand and CarboHSP 40/70

	CarboHSP 40/70	**Sand**
total mass (g)	25	25
orifice diameter (mm)	5	5
discharged mass (g)	21.90 ± 0.02	21.8 ± 0.10
AOR (°)	32.01 ± 0.65	36.85 ± 0.17

AOR was measured via image processing to measure it correctly. After pouring the particles through the orifice and obtained the particle cone, photos of the particle cone were taken. Camera position, focal length and focus point were adjusted. To discriminate particles from the background, a black background was used for sand particles, and white background was used for CarboHSP 40/70 particles. Particle locations on both sides of the cone on the x-y plane were recorded by image processing. Then, two lines were fitted on both sides according to recorded particle coordinates. The slope of these lines gives AOR. The mean value of right and left AOR was taken. The standard deviation of AOR measurements for CarboHSP 40/70 is 2 %, for sand particles is 0.46 %. Figure 3.8 shows the image processed AOR test result of CarboHSP 40/70 particles.

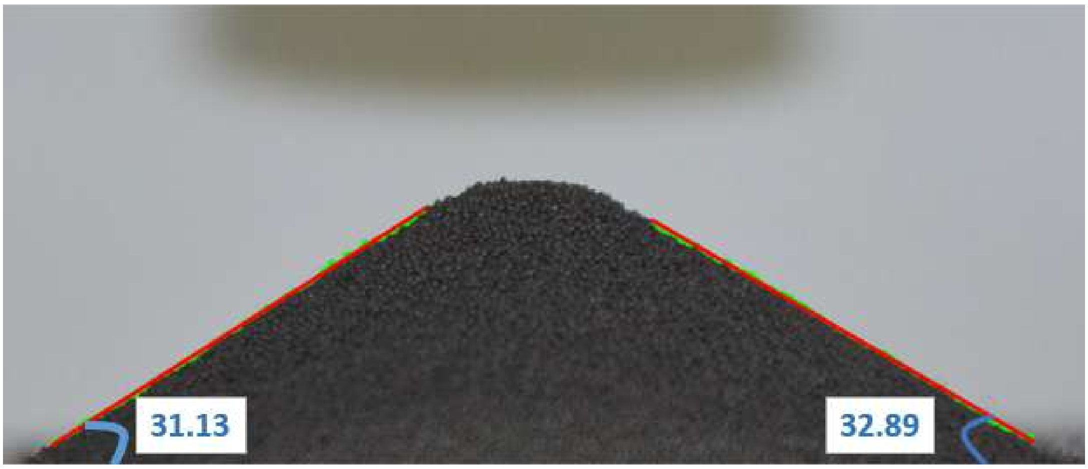

Figure 3.8: AOR measurement of CarboHSP 40/70 particles by using image process

Since a small amount of particles are discharged, the discharged mass was measured by a sensitive laboratory scale to reduce error. Standard deviations of measurements of discharged mass for CarboHSP 40/70 is 0.09 $\%$, and for sand is 0.45 $\%$. Low measurement deviations of AOR and discharged mass show that these tests are repeatable and suitable to use as calibration tests.

3.3.2 DEM Models

The same particle discharge test was modeled on DEM software LIGGGHTS. To reduce simulation time, Young's Modulus E of particles and wall was set to 5x10^6 Pa, which is the smallest allowable E on DEM according to the used Hertz- Mindlin contact model. Simulation time steps are adjusted according to the smallest particle diameter in the simulation. In the modeling of CarboHSP 40/70 particles, the smallest particles that occupy the least volume (Figure 3.2) were excluded to speed up simulations. ν was set to 0.3. e_{p-p} and e_{p-w} were kept constant, as stated in Table 3.7.

A flat plate was set 4 cm below the orifice. Investigated wall friction coefficients μ_{p-w} and $\mu_{r,p-w}$ were assigned to it. Particles were filled in the metal funnel and waited up to mean particle kinetic energy is in the order of e^{-13} $\mathrm{kg\,m^2/s^2}$ to be sure that particles settle down and then particles were allowed to discharge from the orifice. Particles formed a pile on the metal surface, and computation was stopped when particles' mean kinetic energy is in the order of e^{-15} $\mathrm{kg\,m^2/s^2}$. Discharged mass was recorded by DEM code during discharge. To measure AOR from DEM, post-processing was performed by Paraview visualization software. Camera settings and position were adjusted as the same as the performed real-life test. A screenshot of the formed particle cone was taken. The image processing on MATLAB was applied to photos of particle cone, and AOR was determined.

3.3.3 Numerical Sensitivity Tests on DEM

Sensitivity test is a common method for the DEM calibration approach. Different macro measurements are sensitive to different micro material properties. In order to understand which micro material parameters affect the AOR and discharge time, the sensitivity test was applied on a numerical discharge test. Thus, effects of micro properties were checked. While changing a certain parameter, other parameters were kept constant to understand its impacts on bulk response. Table 3.6 shows the values of parameters used in the sensitivity test. Maximum and minimum values of inter-particle friction coefficients and particle-wall and particle-particle restitution coefficients were examined, and results are shown in Figures 3.9 and 3.10. Horizontal lines in the middle of the graphs represent the real-life test results. Blue bars show the simulation results of an investigated parameter when it has its highest value. Similarly, orange bars show the simulation results of an examined parameter when it has its lowest value.

The sensitivity test showed that friction coefficients are the most effective parameters on AOR and discharged mass. It can be said that these tests are suitable for the calibration of inter-particle friction coefficients. Effect of particle-particle and particle-wall restitution coefficients are less compared to inter-particle friction coefficients. Since restitution coefficients will be kept constant during calibration, the effect of them will be insignificant.

Table 3.6: Particle interaction parameters used in sensitivity test

	Fixed Parameter	**Variable Parameter (Min, Max)**
μ_{p-p}	0.7	0.1, 0.9
$\mu_{r,p-p}$	0.3	0.1, 0.5
e_{p-p}	0.5	0.1, 0.9
e_{p-w}	0.6	0.1, 0.9

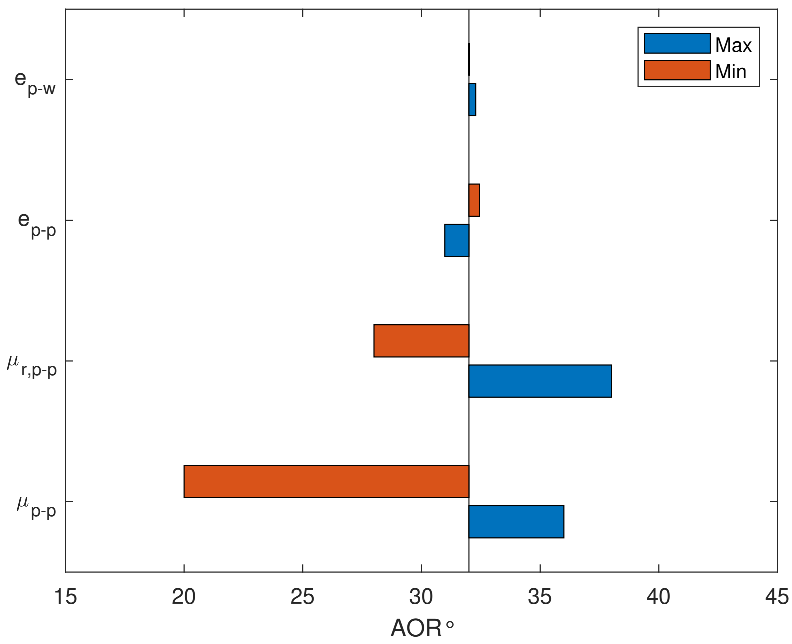

Figure 3.9: The effect of the parameters on the angle of repose of CarboHSP 40/70

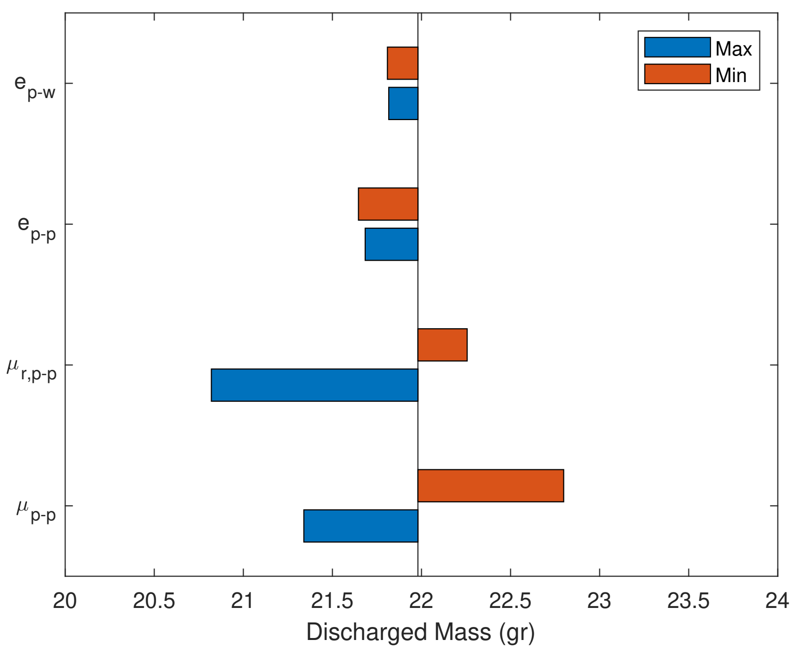

Figure 3.10: The effect of the parameters on the discharged mass of CarboHSP 40/70

3.3.4 Calibration Stage

All of the other properties were kept constant in DEM model except for μ_{p-p} $\mu_{r,p-p}$, as can be seen in Table 3.7. Contour graphs for AOR and discharged mass can be seen in Figures 3.11 and 3.12 for possible parameter sets.

Table 3.7: Particle and interaction properties used in inter-particle friction coefficient calibration tests

	CarboHSP 40/70	**Sand**
Poisson's Ratio		
Particle	0.3	0.3
Wall	0.3	0.3
Young's Modulus		
Particle	$5x10^6$ Pa	$5x10^6$ Pa
Wall	$5x10^6$ Pa	$5x10^6$ Pa
Restitution Coefficient		
Particle-Particle	0.5	0.5
Particle-Wall	0.6	0.6
Sliding Friction Coefficient		
Particle-Particle	0.1-0.9	0.1-0.9
Particle-Wall	0.43314	0.39619
Rolling Friction Coefficient		
Particle-Particle	0.1-0.5	0.1-0.5
Particle-Wall	0.12757	0.15974

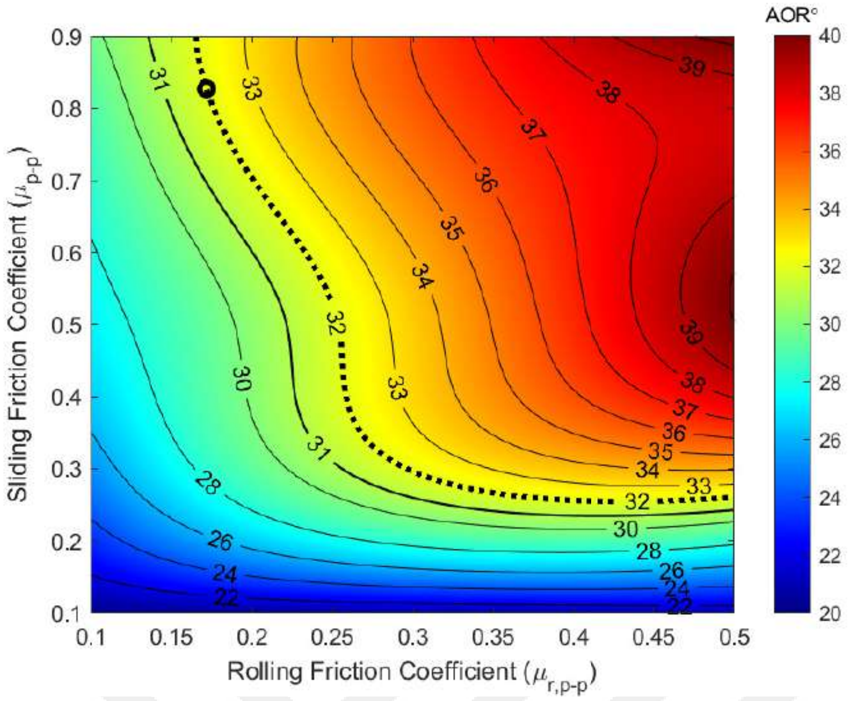

Figure 3.11: AOR contour graph for mono-size DEM model of CarboHSP 40/70

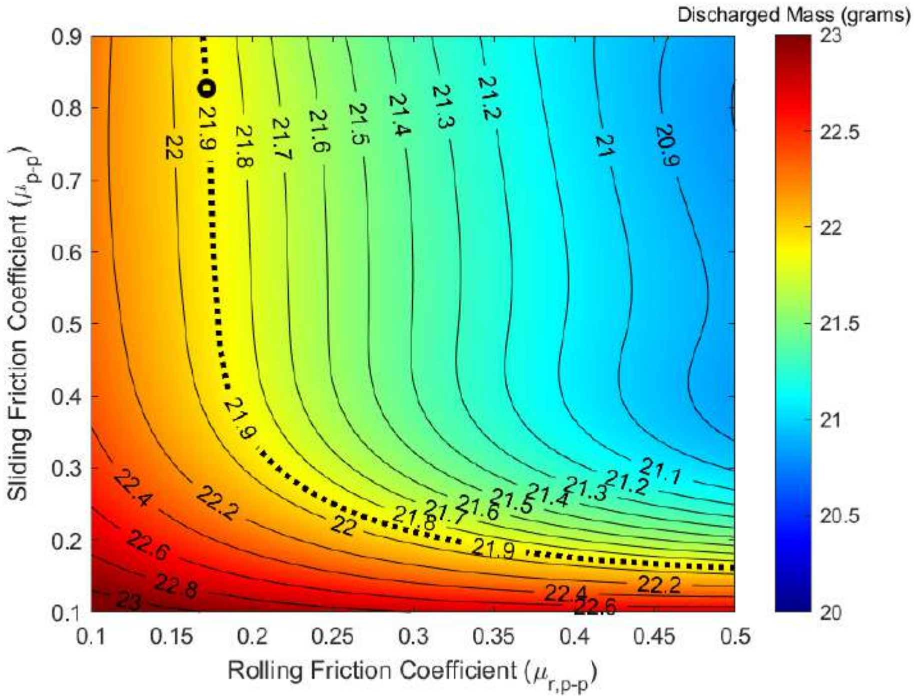

Figure 3.12: Discharged mass contour graph for mono-size DEM model of CarboHSP 40/70

As can be seen from Figure 3.12, discharged mass decreases with increasing friction coefficients. When friction coefficients are high, more particles stay above the orifice by keeping each other. $\mu_{r,p-p}$ is not effective on discharged mass for low sliding friction coefficients (μ_{p-p} is less than 0.35). Dominant friction effect arises from the sliding force. However, for high μ_{p-p}, the effect of $\mu_{r,p-p}$ becomes much important for discharged mass. When both friction coefficients are high, the largest amount of particles kept above the orifice and discharged mass is the lowest. Discharged mass is more sensitive to μ_{p-p} when μ_{p-p} < 0.35, which is consistent with the sensitivity study performed in the previous section. However, when μ_{p-p} is high (greater than 0.35), rolling friction is the dominant factor on the discharged mass amount.

Although it seems that there is not much difference between the maximum and minimum contour lines of Figure 3.12, calibration can be performed accurately. This is because measurement deviations are small in the order of 10^{-2} g.

One can notice from Figure 3.11, AOR increases with friction coefficients. Same as discharged mass characteristics, rolling friction is not effective on AOR for low μ_{p-p} values. AOR is highly sensitive to μ_{p-p} for its low values. Unlike discharged mass, AOR is also quite sensitive for high μ_{p-p}. Thus, for high μ_{p-p}, both rolling and sliding frictions are effective on AOR.

AOR contours alter in a wide range compared to discharged mass graphs. Measurement deviations are small compared to the wide range of contour, so it does not affect the calibration results.

Real-life test results are shown as dashed contours on graphs. As can be seen from contour graphs, many different parameter sets give the same results. So, it is not possible to determine the accurate parameter set by only one measurement. Combining both graphs, the intersection of real measurement results gives the correct parameter set that fulfills both measurements were obtained. Marked calibration results can be seen on the measurement contour lines. Mean values of measurement contours intersect at one point. Measurement deviations do not cause any difference in results. This shows that the calibration of friction coefficients is reliable.

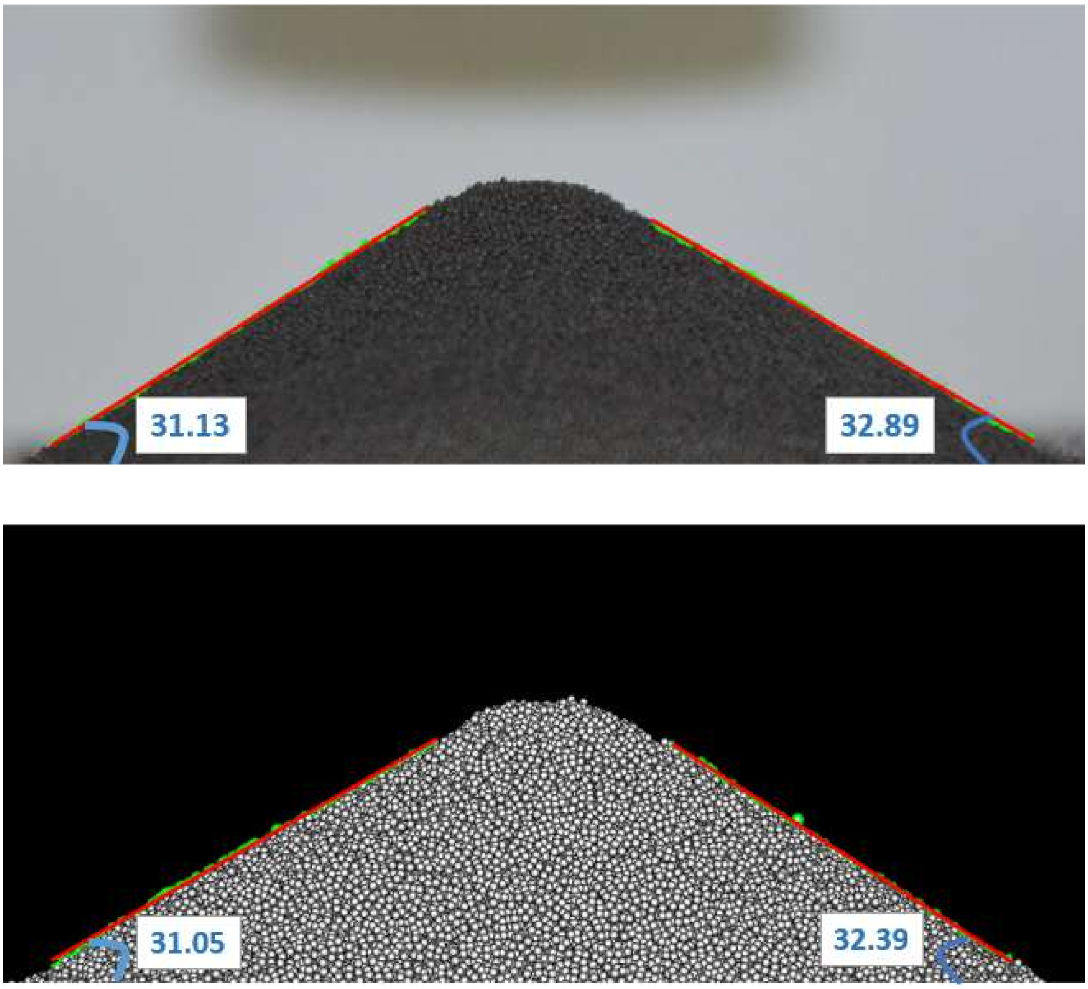

Figure 3.13: AOR measurement of CarboHSP 40/70 particles: test (top) and DEM model (bottom)

Figure 3.13 shows the comparison of real-life AOR and validated mono-size DEM model AOR. One can notice from Figure 3.13 slope of the lines seems nearly identical. Related results will be discussed in Section 3.7.

3.4 Mono Size and Multi Size Particle Modelling Comparison

Friction coefficient calibration was performed for both mono and multi-size particle models. For CarboHSP 40/70, multi-size model particle sizes were adjusted according to Figure 3.2 with the exclusion of the smallest size particles. In the mono-size particle model, particle diameter was set to 440 $\mu\mathrm{m}$ which is 55 $\mu\mathrm{m}$ larger than the measured mean diameter to compensate for the exclusion of the smallest particles. The multi-size model includes very small particles. DEM time step is adjusted according to the smallest particle in the simulation domain. Thus, one should notice that multi-size modeling is computationally costly compared to the mono-size model.

Contour graphs of discharged mass and AOR of multi-size model CarboHSP 40/70 are shown in Figures 3.14 and 3.15. One can notice from Figures 3.14 and 3.15 characteristics of the AOR and discharged mass contour graphs of the multi-size model seems quite alike with mono-size contours. This shows multi-size and mono-size models behave similarly with the same particle property sets. Calibration results for both multi-size and mono-size CarboHSP 40/70 particles can be seen in Table 3.8. Calibrated inter-particle friction coefficients are quite similar. This might be because particles are nearly spherical, and particle sizes do not vary in a wide range. It can be said that mono-size models can be utilized for ease of computation of CarboHSP 40/70 particles.

The discharged mass contour graph for the multi-size model shows all of the characteristics of the mono-size graph stated in the previous section. Multi-size model AOR contour also has almost all of the characteristics of the mono-size model. In addition, for μ_{p-p} values are in between 0.35 and 0.7 multi-size model, AOR is not sensitive to sliding friction; rolling friction is dominant on AOR for that interval. For higher sliding friction coefficients (μ_{p-p} > 0.7), sliding friction is effective on the discharged mass in addition to rolling friction.

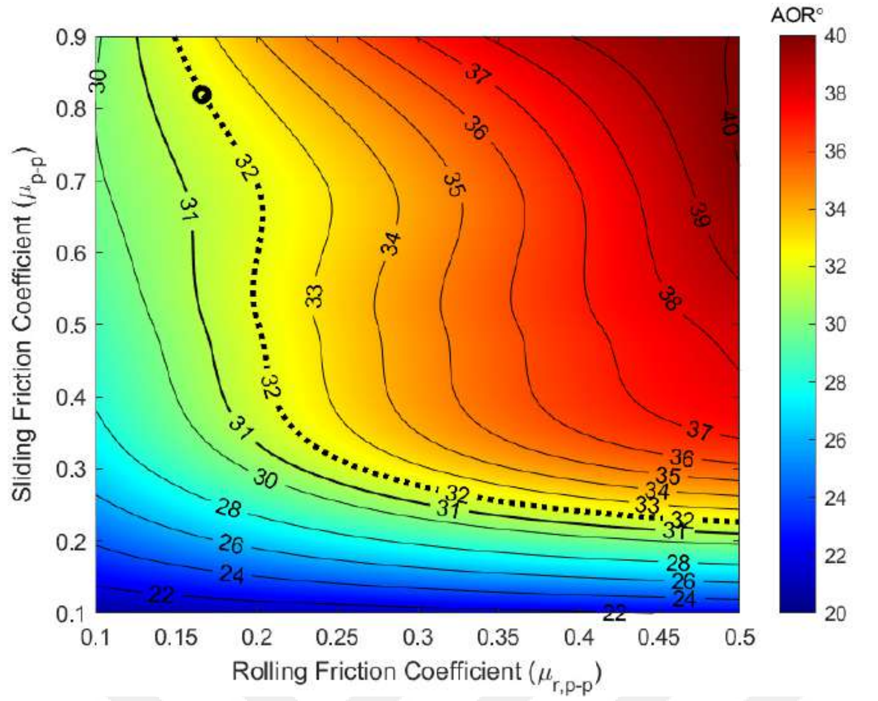

Figure 3.14: AOR contour graph for multi-size DEM model of CarboHSP 40/70

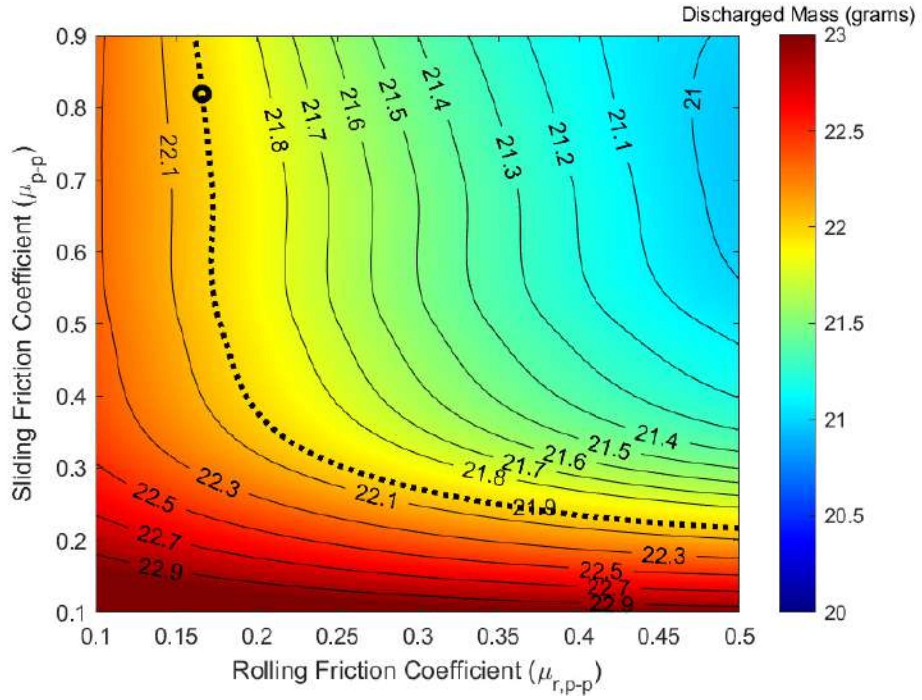

Figure 3.15: Discharged mass contour graph for multi-size DEM model of CarboHSP 40/70

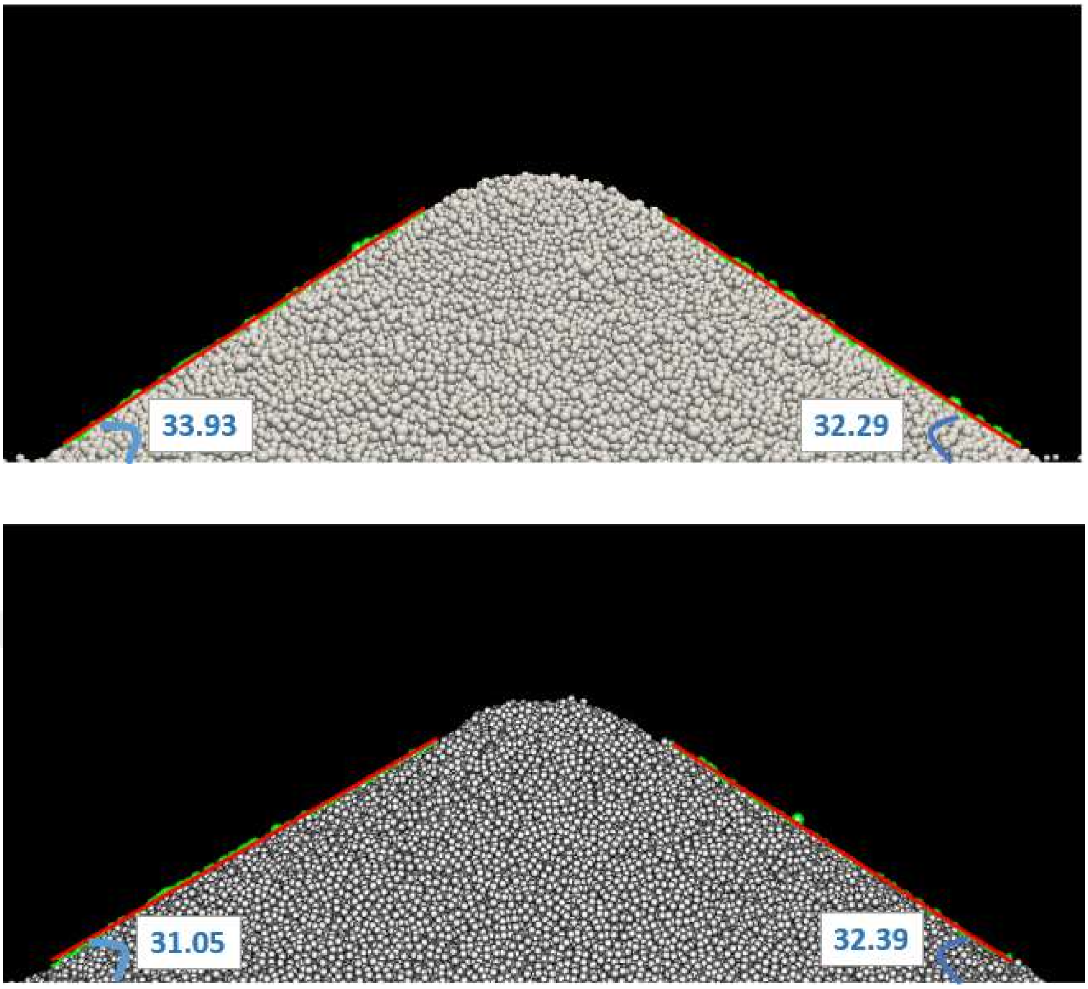

Figure 3.16: AOR measurement of CarboHSP 40/70 particles: multi-size model (top) and mono-size model (bottom)

In figure 3.16 comparison of AOR mono and multi-size DEM model for CarboHSP 40/70 is presented. DEM models are performed with validated friction coefficients. As one can notice from Figure 3.16 slope of the lines seems close to identical. Detailed results will be discussed in Section 3.7.

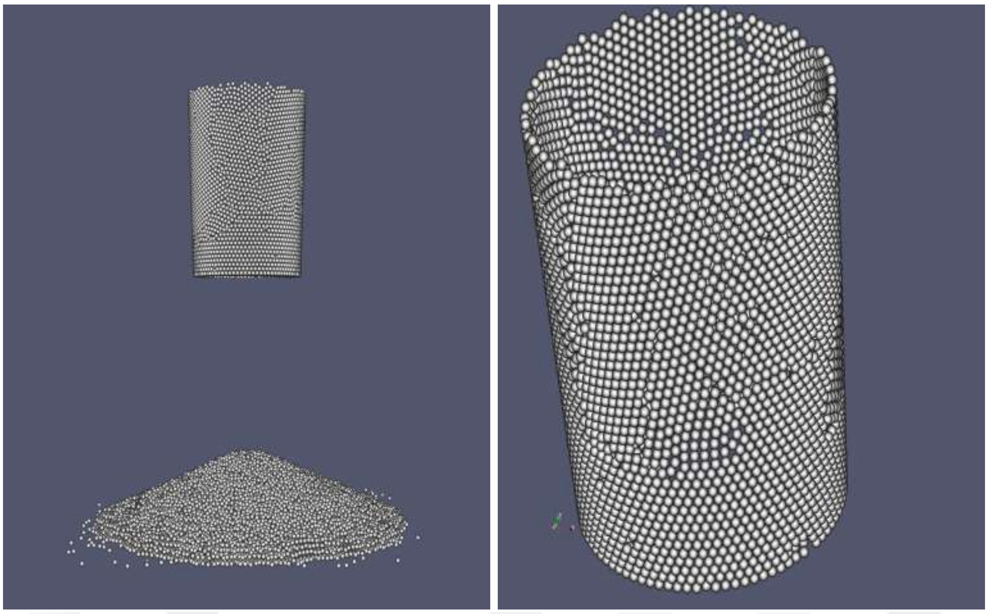

Figure 3.17: Simulation results from failed mono-size DEM model of sand particles

765 μm size particles were utilized for mono-size modeling of the sand particles. However, mono-size particles showed unrealistic behavior. They composed a mono-layer inside the funnel wall, as shown in Figure 3.17. This layer developed independently of friction coefficients between particles. Comparing the CarboHSP 40/70 particles, sand particles are found to be unsuitable for mono size modeling. This is because of the irregular shapes of sand particles. Unlike CarboHSP 40/70 particles, particle interaction does not compensate for the shape irregularity and multi-size structure of the sand particles.

3.5 Inter-particle Friction Coefficient Calibration of Sand Particles

Calibration of sand was performed with multi-size particle models. Particle size distribution is adjusted according to Figure 3.3, and any exclusion was not done since the smallest particle diameter allows an appropriate time step. In Figure 3.18, test and DEM model comparison can be seen.

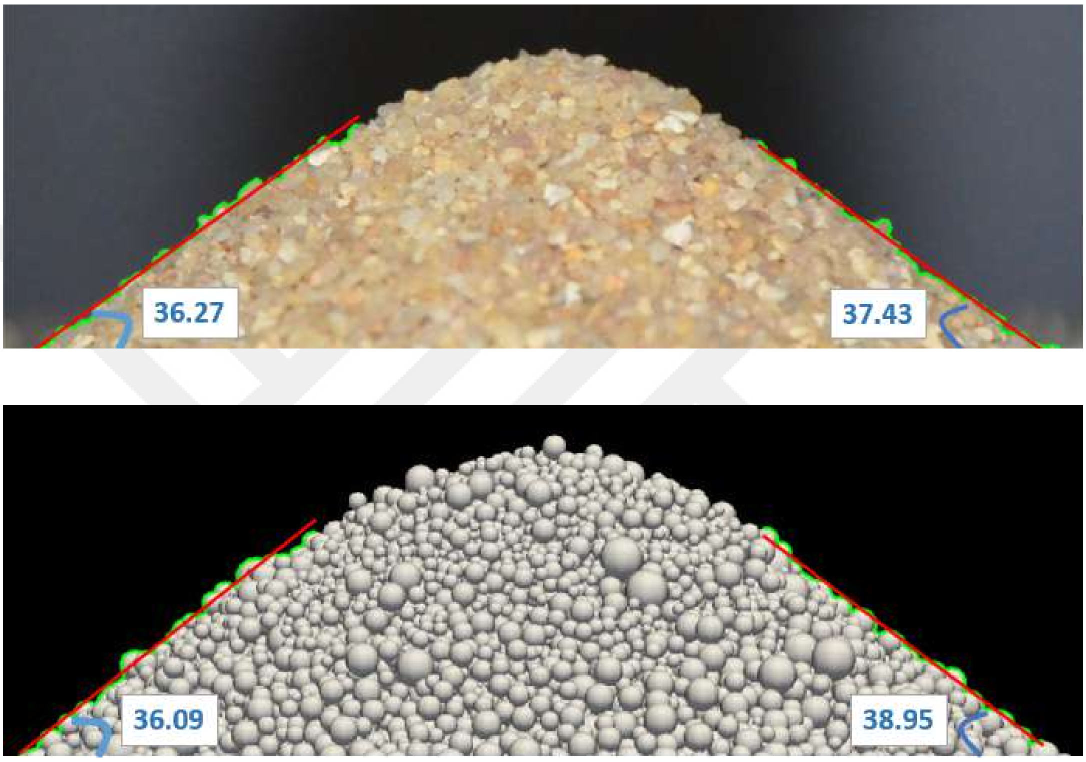

Figure 3.18: AOR measurement of sand particles: test (top) and DEM model (bottom)

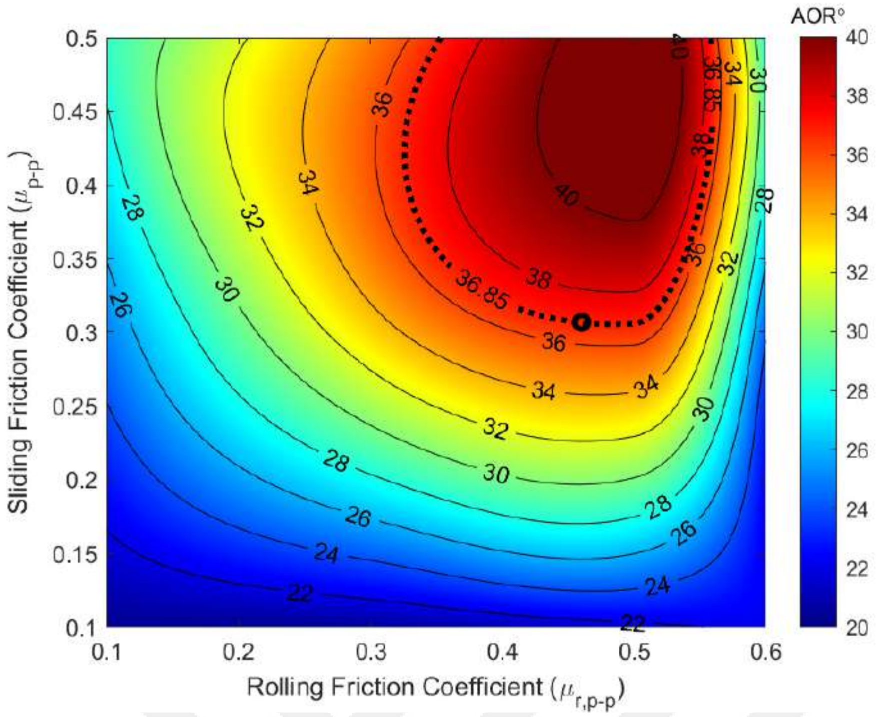

Figure 3.19: AOR contour graph for multi-size DEM model of sand

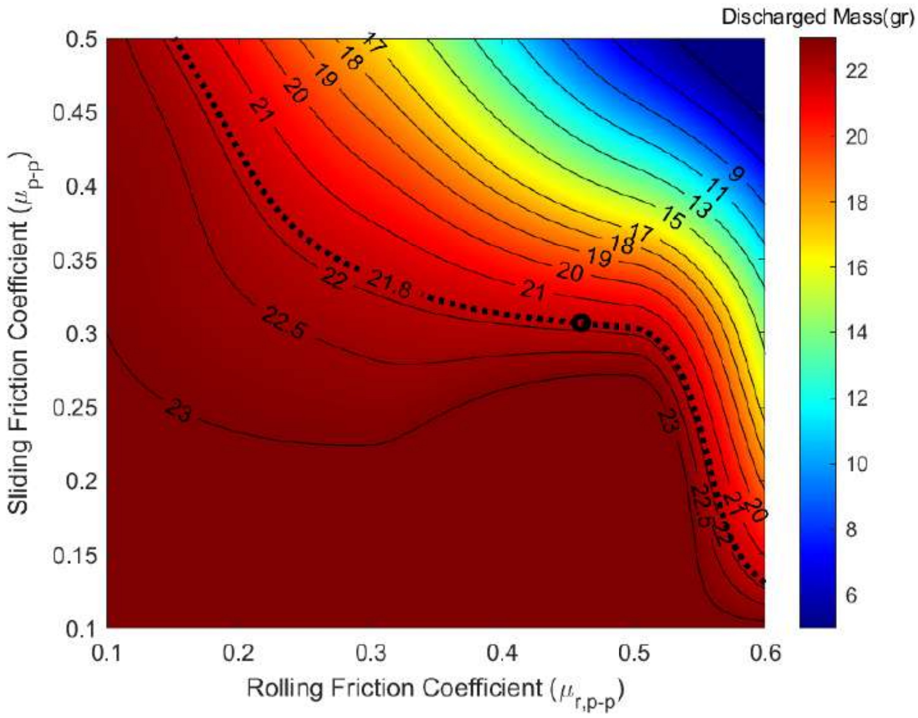

Figure 3.20: Discharged mass contour graph for multi-size DEM model of sand

Discharged mass and AOR contour graphs of multi-size DEM models of sand particles can be seen in Figures 3.19 and 3.20. DEM simulations were performed up to values 0.5 for μ_{p-p} and 0.6 for $\mu_{r,p-p}$. After these values, the orifice plugged totally, and any particles did not flow from the orifice. Compared to CarboHSP 40/70, sand includes bigger sizes of particles. When these bigger size particles have high friction coefficients, they clog the 5 mm orifice.

AOR and discharged mass contour graphs of sand particles show different characteristics from CarboHSP 40/70 particles' contour graphs. Both types of particles were modeled as perfect spheres. However, CarboHSP 40/70 particles' sizes are distributed in a narrower range, while the sand grains' sizes are distributed in a broader range. The difference in the particle size distribution range affects the contour graphs' characteristics.

In Figure 3.19, it is seen that AOR contour lines gradually increase as an almost circular shape. The circular shape of the contour lines shows that the multi-size DEM model of AOR of sand particles is highly sensitive to the μ_{p-p} and $\mu_{r,p-p}$, especially for high friction coefficients. AOR increases while friction coefficients get high. Since blockage started at high friction coefficients, the highest possible friction coefficient pair could not result in maximum AOR. After reaching maximum AOR, if friction coefficients increase, AOR starts to decrease because of the low amount of discharged particles.

When μ_{p-p} is lower than 0.2, AOR does not change with $\mu_{r,p-p}$. $\mu_{r,p-p}$ become effective on AOR for values μ_{p-p} is higher than 0.2. AOR contour lines are nearly vertical when $\mu_{r,p-p}$ is higher than 0.55; thus, μ_{p-p} does not influence the AOR. Measurement result contour is in the place that μ_{p-p} and $\mu_{r,p-p}$ are both effective on it. However, the circular shape of the contour deviation of measurement cause ambiguity in the calibrated rolling friction when AOR contour is coupled with discharged mass contour. To prevent ambiguity, number of discharged test was increased to reduce the deviation.

Discharged mass decreases with increasing friction coefficients. Unlike CarboHSP 40/70, a very low amount of mass was discharged at high friction coefficients due to orifice blockage. For low friction coefficient pairs, discharged mass contour lines do not alter in a wide range; as friction coefficients increase, the interval of contour lines increases. Discharged mass is sensitive to both μ_{p-p} and $\mu_{r,p-p}$ for higher friction coefficients couples. The measurement contour line is in the place that friction coefficients are effective on it. Since the deviation of the measurement is low, it does not alter the contour line. However, the gradient of measurement contour is low when $\mu_{r,p-p}$ is between 0.3 and 0.5, which caused an ambigıuty in the calibration of rolling friction as mentioned above.

Calibrated inter-particle friction coefficients can be seen in Table 3.8. As mentioned before, mono-size and multi-size model calibration results of CarboHSP 40/70 particles are nearly identical. As expected, $\mu_{r,p-p}$ of sand particles is higher than CarboHSP particles. Sphericity of the sand particles is quite low, shape compensation effect seen on rolling friction calibration. However, CarboHSP 40/70 particles are highly spherical, shape compensation on rolling friction is less than sand particles; thus, the $\mu_{r,p-p}$ of CarboHSP 40/70 is way lower than sand. μ_{p-p} of CarboHSP 40/70 particles are higher than sand particles. This shows that μ_{p-p} only depends on the material properties; it is not affected by the particles' shape.

Table 3.8: Calibrated particle-particle friction coefficients

	CarboHSP 40/70 (Mono-Size)	**CarboHSP 40/70 (Multi-Size)**	**Sand (Multi-Size)**
μ_{p-p}	0.827	0.819	0.307
$\mu_{r,p-p}$	0.172	0.166	0.462

3.6 Calibration of Restitution Coefficients

There is no robust calibration method in the literature for the investigation of restitution coefficients of particle-particle e_{p-p} and particle-wall e_{p-w}. One of the most commonly used methods is the direct measurement of restitution coefficients with the drop test. However, this method is not accurate since utilized particles in real life are not perfectly spherical, and each has different shapes and sizes. Thus, a new method for easy investigation of restitution coefficients is presented in this section.

3.6.1 Hands on Test

The discharge test was performed, and the scattering of particles on a metal surface was examined. Particles were poured from the same metal funnel setup, which was used for inter-particle friction calibration to the metal plate, which is placed 4 cm away from the orifice. Same orifice diameters were used in the discharge test. Scattering occurs because particles gain high kinetic energy when dropping from the orifice. Firstly dropped particles collide with the metal wall and scatter on the surface. Then, particle pile forms, and dropped particles bounce on the pile by colliding other particles and scatter on the metal surface.

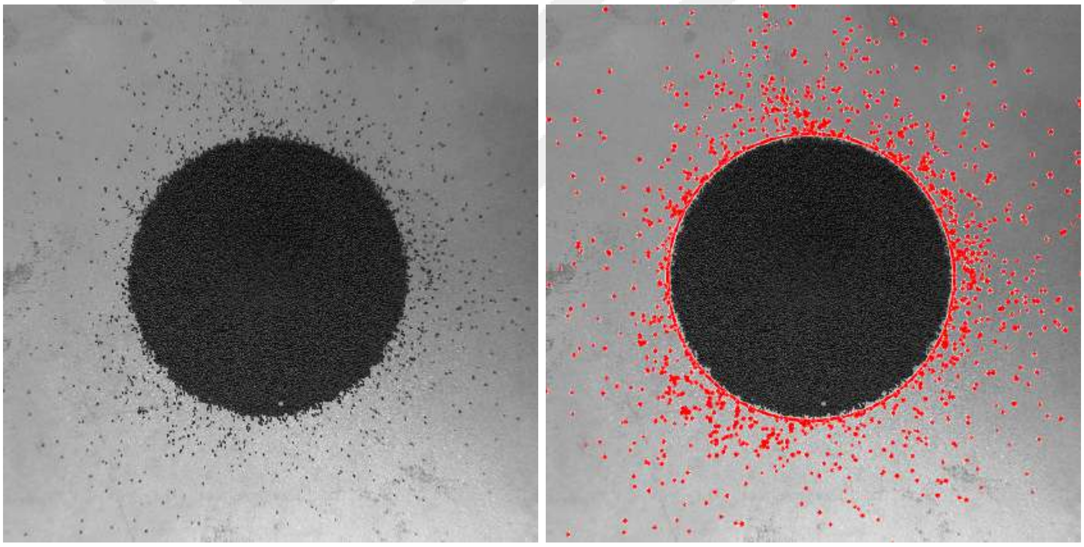

Figure 3.21: Particle scattering of CarboHSP 40/70 before image processing (left) and after image processing (right)

A top view photo of the particle cone and scattered particles was taken. Figure 3.21 shows the top view of the formed particle pile and scattered particles around it as a result of the discharge test. The bottom diameter of the particle pile was determined via image processing. This diameter of the pile was defined as an area in which the existing density of particles is high. As shown in Figure 3.21 scattered particles that are beyond the pile bottom diameter were counted via image processing. Scattering test was repeated 6-8 times, related results can be seen in Table 3.9.

3.6.2 DEM Model

The same discharge test was repeated with varying restitution coefficients on DEM for both CarboHSP 40/70 and sand particles. The simulation box was kept larger than previous discharge simulations to entirely observe all scattered particles on the 10x10 cm^2 plate for CarboHSP 40/70 and 10x10 cm^2 plate for sand. Metal plate distance from the orifice might affect the scattering since particles' gained energy depends on the dropping height. Thus, plate distance was adjusted according to the real-life test.

Same as friction coefficients calibration simulations Young's Modulus E was set to the smallest allowable value (5x10^6 Pa) and Poisson's ratio ν is taken as 0.3 for both wall and particles. Previously obtained friction coefficients μ_{p-p}, μ_{p-w}, $\mu_{r,p-p}$, $\mu_{r,p-w}$ were set to the DEM model. e_{p-p} and e_{p-w} were varied between 0.1-0.9. Although varying friction coefficients affect the bottom diameter of the particle pile, it is fixed in this calibration due to inserted fixed friction coefficients. Thus, the only effective parameters on scattering are particle-particle and particle-wall restitution coefficients. Since friction coefficients are fixed, the pile's bottom diameter is the same as the real-life test for all restitution coefficient pairs. Scattering measurements were performed based on fixed pile bottom diameter for areas beyond this diameter.

A larger simulation domain increases computation time. Thus, to have reasonable computation time, only the mono-size model has calibrated for restitution coefficient of CarboHSP 40/70 particles. As observed in Section 3.4, mono-sized modeling of sand particles causes unrealistic results, so sand particles are modeled as multi-size. Even though this reduces the computational efficiency, the smallest size of the sand particles allows for a reasonable simulation time step.

3.6.3 Calibration Stage

Scattering amount of particles was examined for 3 different regions on the plate to calibrate precisely both e_{p-p} and e_{p-w}. Figure 3.22 shows the examined areas. Area 1 is the innermost area, defined between the cone diameter and the diameter closest to it. Area 2 is defined between the second smallest circle and the largest circle. Area 3 is defined between the largest circle and boundaries. Sizes of these areas can change according to particles. This will be discussed in the following sections.

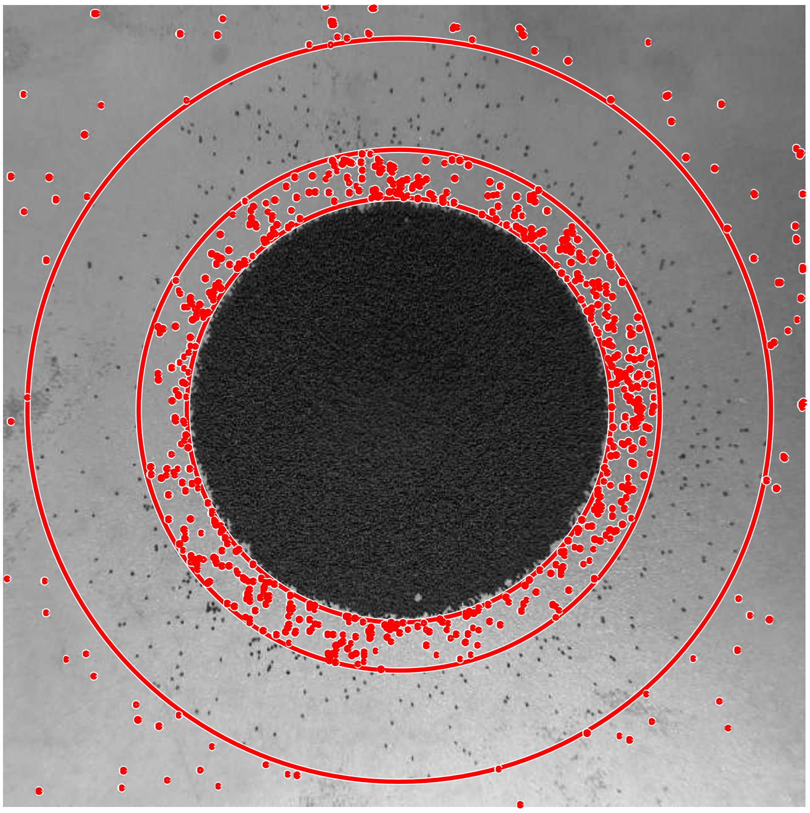

Figure 3.22: Particle scattering of CarboHSP 40/70 on metal plate on the examined areas

Table 3.9 shows the scattering amount of CarboHSP 40/70 and sand particles on different regions. The maximum deviation is 11.65 % for CarboHSP 40/70 and 13.46 % for sand particles. Even though the measurement deviation is high, it is satisfactory for the investigation of the restitution coefficients accurately. This can be explained by the high sensitivity of the scattering test to restitution coefficients.

Table 3.9: Particle scattering measurements for sand and CarboHSP 40/70

	CarboHSP 40/70	**Sand**
total mass (g)	25	25
orifice diameter (mm)	5	5
scattering amount on area 1	652 ± 76	520 ± 55
scattering amount on area 3	75 ± 8	52 ± 7

Figure 3.23 shows contour graph of the particle scattering amount of CarboHSP 40/70 on area 1 with different e_{p-p} and e_{p-w} pairs. As e_{p-p} increasing, scattering becomes more sensitive to it, so contour intervals get larger. Low e_{p-p} values are not as effective as high e_{p-p} on scattering. Thus contour intervals become larger as e_{p-p} increasing. A small change of e_{p-p} alter the scattering amount on area 1 a lot for higher e_{p-p}. However, this is not valid for lower e_{p-p} values than 0.6. Measurement is shown as a dashed black contour in Figure 3.23. Measurement contour is in the region that scattering is quite sensitive to the e_{p-p}. Thus 12.48 % deviations of the scattering measurement on area 1 do not change the calibration result.

Contour lines alter with e_{p-p} only for area 1. Thus, scattering in this region is only dominated by collisions between particles. This shows that particles bounce on the pile while the pile is forming. Then particles drop mostly on this area. Thus, the scattering amount on area 1 calibrates e_{p-p}.

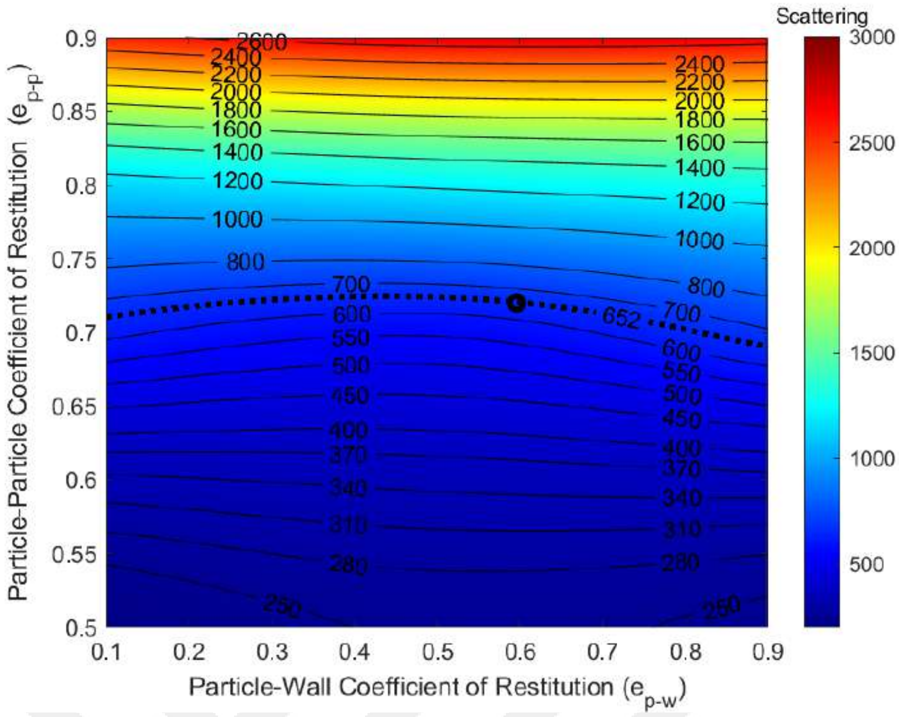

Figure 3.23: Particle scattering amount of CarboHSP 40/70 on area 1

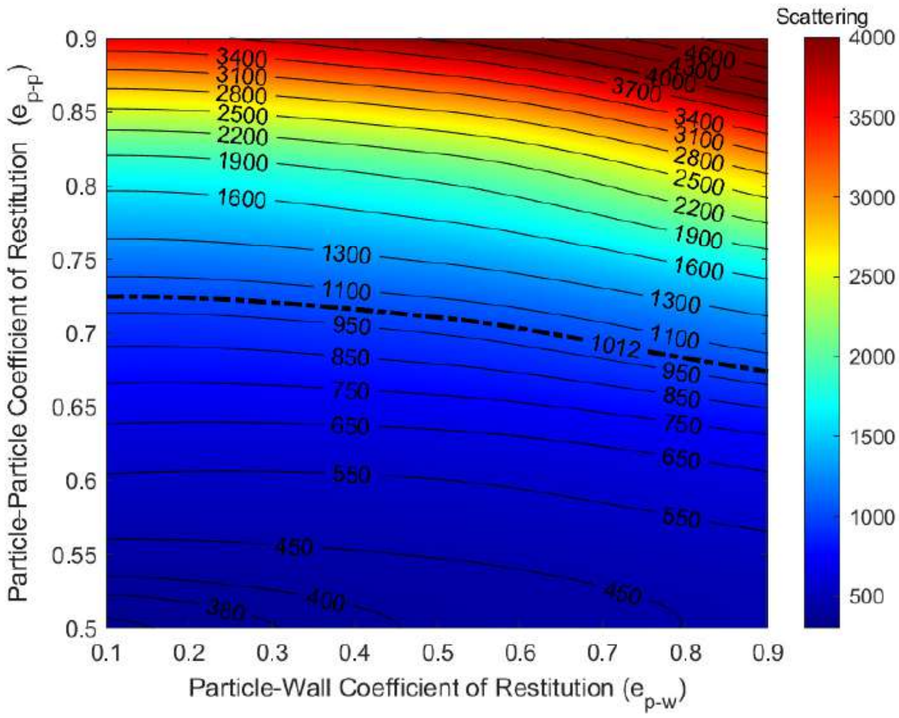

Figure 3.24: Particle scattering amount of CarboHSP 40/70 on widened area 1

As a comparison scenario, area 1 was widened, and particle scattering on this widened area was examined. The contour graph of scattering amount on widened area 1 can be seen in Figure 3.24. As one can notice e_{p-w} shows little effect on a widened area. No matter how large area 1 is (even from the pile diameter to the wall boundaries), e_{p-p} is still the dominant property. e_{p-w} shows a minimal effect compared to e_{p-p} on scattering. It is because the most amount of particles bounce on the pile and then cluster around the pile.

In order to obtain the e_{p-w}, in addition to area 1, area 3 was utilized. Figure 3.25 shows the scattering amount of CarboHSP 40/70 particles on area 3. Scattering becomes more sensitive as higher the e_{p-p} and e_{p-w}. As mentioned before, contour line intervals get larger with small changes of restitution coefficients. Considering the 8 $\%$ deviations of the measurement and contour graph sensitivity, it can be said that measurement deviations on area 3 do not alter the result. As one can notice e_{p-w} is as effective as e_{p-p} on scattering amount on area 3.

Area 3 was widened towards area 2 by keeping metal plate boundaries constant. Figure 3.26 shows particles scattering on widened area 3. Obviously, e_{p-w} is becoming less effective as area 3 widened towards the particle cone. This is because more particles that are scattered as a result of particle-particle bouncing are included when the area gets closer to the particle pile.

The increasing effect of e_{p-w} on area 3 can be explained as follows. Some particles that are reached near the boundaries bounce more than once. Firstly they bounce on the particle pile and then bounce on the wall, especially on area 2 and then reach area 3. This explains the dominant effect of e_{p-p} on scattering for all regions and the increasing effect of e_{p-w} while getting far away from the pile.

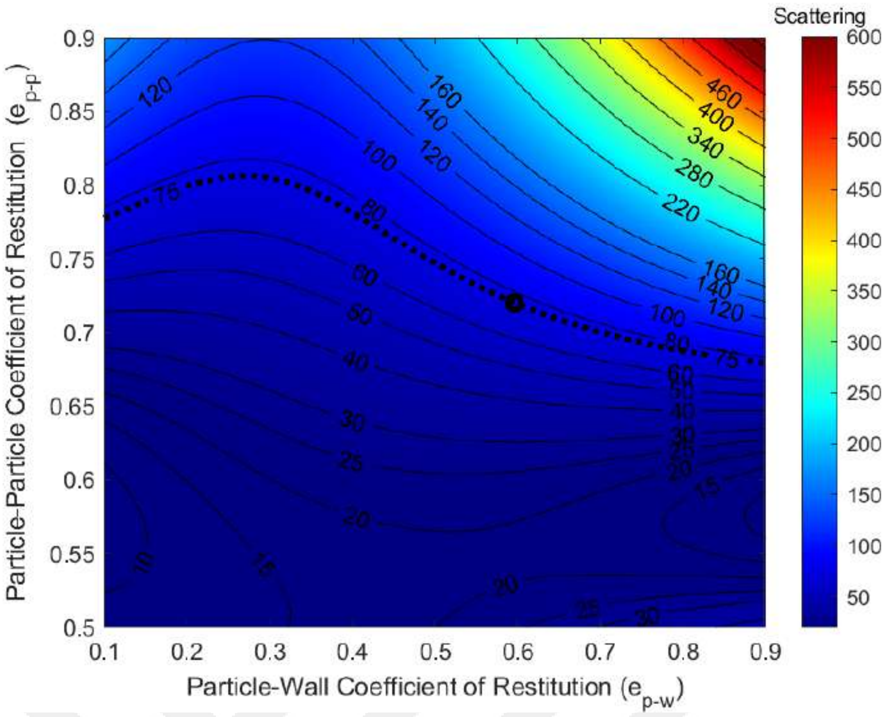

Figure 3.25: Particle scattering amount of CarboHSP 40/70 on area 3

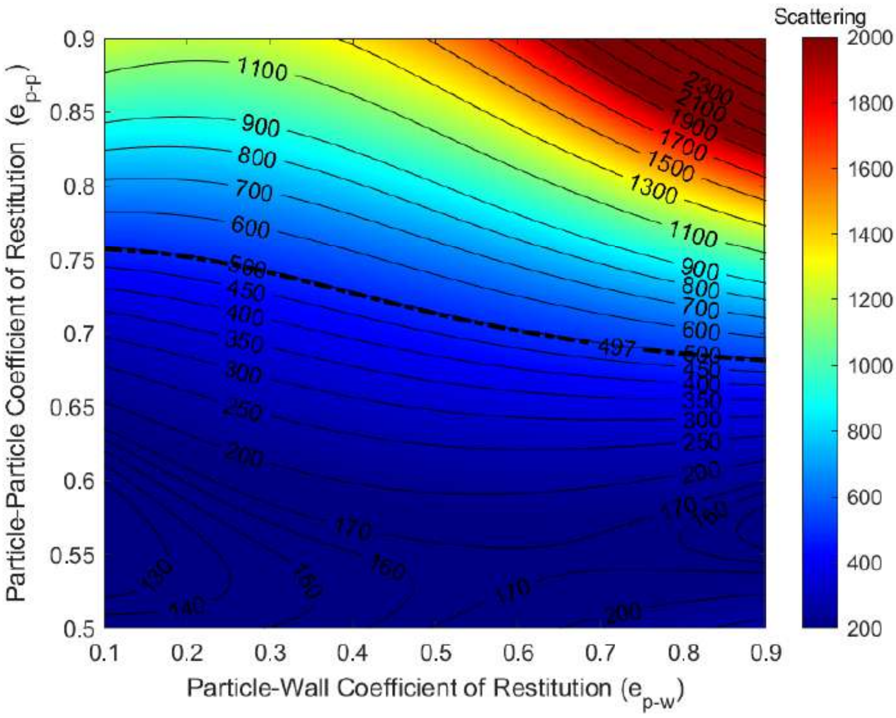

Figure 3.26: Particle scattering amount of CarboHSP 40/70 on widened area 3

Considering all mentioned above, it is concluded that scattering amount on area 1 and area 3 should be utilized for proper investigation of e_{p-p} and e_{p-w}. If one uses area 1, only e_{p-p} could be obtained. In addition, the scattering amount on area 3 should be utilized because it is the area where the scattering amount is most sensitive to the e_{p-w}. Measurement and calibration results of CarboHSP 40/70 particle scattering are shown in Figures 3.23 and 3.25 as dashed lines and highlighted points. Scattering amount comparison of the test and verified DEM model is shown in Figure 3.27.

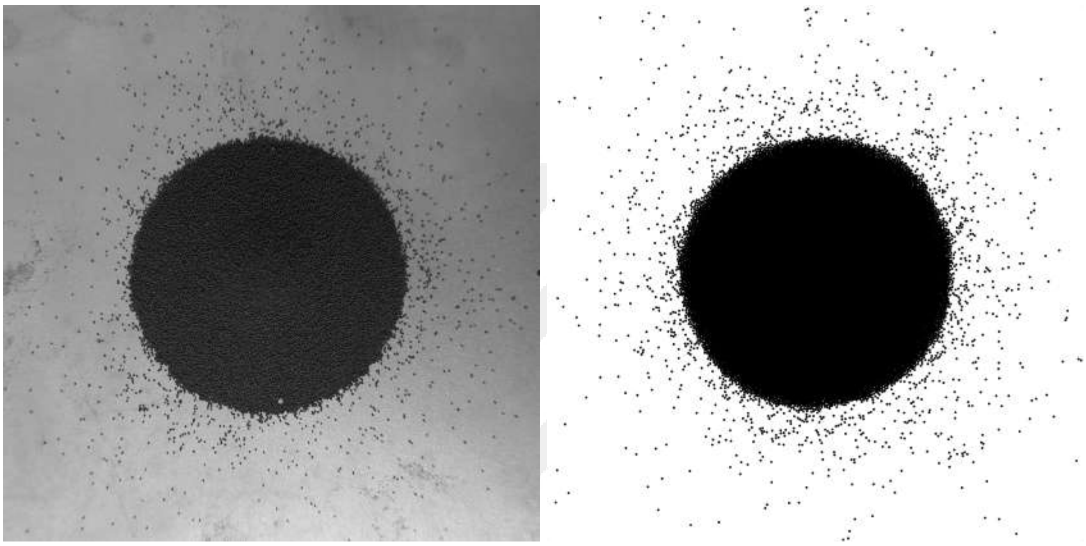

Figure 3.27: Particle scattering comparison of test (left) and DEM model (right) for CarboHSP 40/70

The same test and calibration procedure applied to the CarboHSP 40/70 particles were applied to the sand particles. Sand particle pile's bottom diameter is larger compared to CarboHSP 40/70. Thus, sand particles were poured on a bigger metal plate (14x14 cm^2) to distinguish area 1 and area 3. Area 1 and area 3 were chosen by varying areas in the preliminary trials. Sizes of area 1 and area 3 can be changed according to particle size and size distribution. However, for different particle types, using innermost (area 1) and outermost area (area 3) for e_{p-p} and e_{p-w} calibration is suitable.

Contour graphs of the scattering amount of sand particles on areas 1 and 3 are seen in Figures 3.29 and 3.30. As mentioned in the 40/70 calibration, e_{p-p} is dominantly effective on the scattering amount on area 1. The sensitivity of the scattering amount is increasing with increasing e_{p-p}. Measurement contour for area 1 is shown as a dashed line in Figure 3.29. Measurement deviation does not affect the calibration result since contour intervals are large enough to compensate for the measurement deviation.

The scattering amount contour graph on area 3 can be seen in Figure 3.30. Scattering is increasing with increasing e_{p-p} and e_{p-p}, because both e_{p-p} and e_{p-p} are effective on scattering amount. The dashed line shows the measurement contour. Measurement deviation is small, so it does not affect the measurement and calibration result. Calibrated e_{p-p} and e_{p-p} values for sand particles is shown as highlighted points in Figures 3.29 and 3.30. Also, scattering comparison of test and verified DEM model for sand particles can be seen in Figure 3.28.

Figure 3.28: Particle scattering comparison of test (left) and DEM model (right) for sand

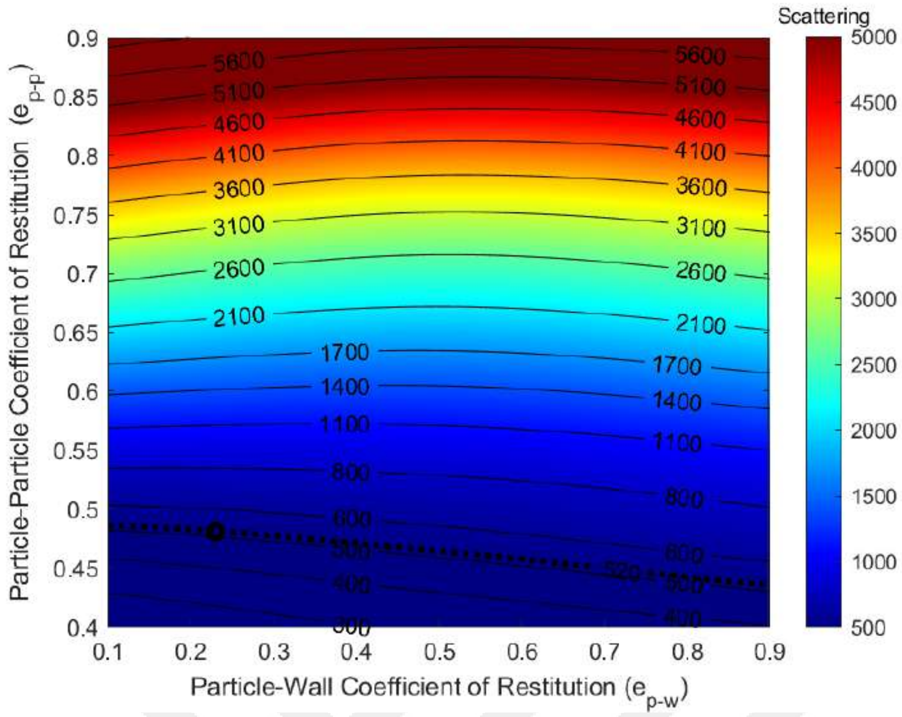

Figure 3.29: Particle scattering amount of sand on area 1

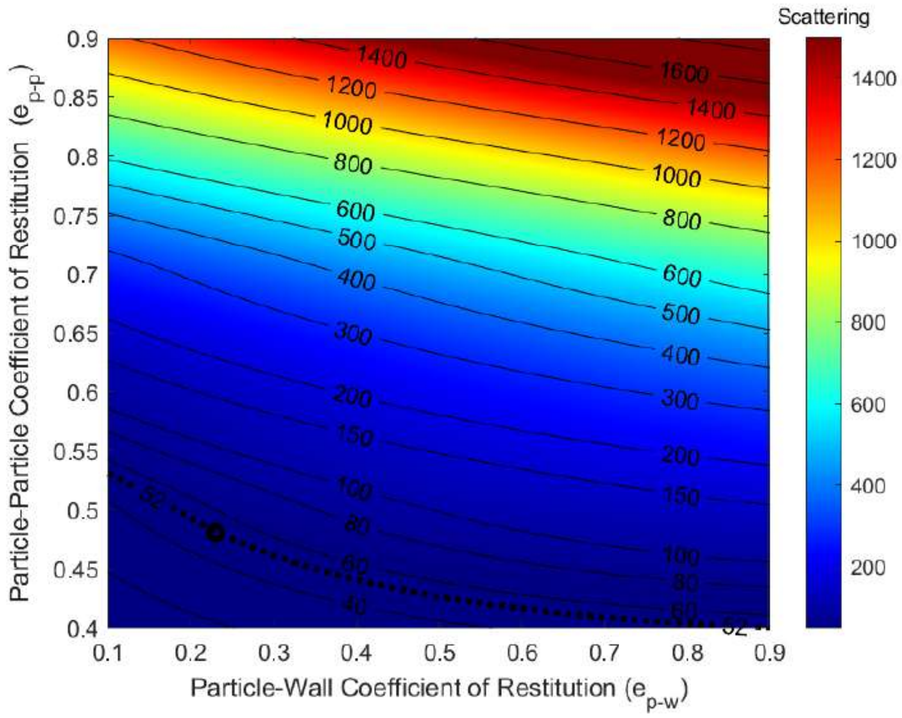

Figure 3.30: Particle scattering amount of sand on area 3

Table 3.10 shows the investigated e_{p-p} and e_{p-w} for CarboHSP 40/70 and sand particles. Sand particles have lower e_{p-p} and e_{p-p} values compared to CarboHSP 40/70 particles. As mentioned in the introduction section, e is an important parameter while designing a particle HEX for heat transfer or storage systems. It directly affects the hydrodynamic behavior of the HEX. Previous experimental bubblized fluidized bed HEX study with the same sand and CarboHSP 40/70 particles performed by Polat [54], supports the findings on restitution coefficients in this thesis. Results of this study show that CarboHSP 40/70 particles have higher bed expansion ratios than sand particles. Difference between the e_{p-p} values of these particles is effective on this result. High e_{p-p} values lead to low energy dissipation between particles. Since particles keep their energy, this results in a high bed expansion ratio [55].

Table 3.10: Calibrated restitution coefficients

	CarboHSP 40/70 (Mono-Size)	**Sand (Multi-Size)**
e_{p-p}	0.71	0.48
e_{p-w}	0.60	0.23

3.7 Validation and Errors

In order to validate the investigated particle properties, the discharged test was repeated with calibrated particle properties on DEM. Comparison of DEM verification results for AOR, discharged mass and scattering measurement with tests and error values are shown in Table 3.11.

Small error values of validation studies show that particle properties are accurately investigated. Percentage errors of AOR are maximum 3.44 $\%$, which contributes to AOR is a common proper measurement for inter-particle friction coefficient calibration. Discharged mass error values are minimal with a maximum 0.45 $\%$, which shows that utilizing discharged mass measurement as a second calibrating bulk property is appropriate. Error values for scattering amount on area 1 seem large for both particle types. Since the error is nearly at the level of standard deviation for CarboHSP 40/70 particles, this error is acceptable. The large error of sand particles can be attributed to the high sensitivity of the area 1 contour to the e_{p-p}. One can notice that the contour graph of area 1 has a higher gradient in the varying e_{p-p} direction for sand compared to CarboHSP 40/70. Thus, a larger error could be expected for the calibration of sand particles.

Table 3.11: Validation and error of calibration results

	CarboHSP 40/70 (Mono-Size)	**CarboHSP 40/70 (Multi-Size)**	**Sand (Multi-Size)**
Discharged Mass			
DEM (g)	21.93	21.95	21.9
Test (g)	21.90	21.90	21.8
Error (%)	0.13	0.23	0.45
AOR			
DEM (°)	31.27	33.11	37.52
Test (°)	32.01	32.01	36.85
Error (%)	2.31	3.44	1.81
Scattering Amount (Area 1)			
DEM	576	-	613
Test	652	-	520
Error (%)	11.66	-	17.88
Scattering Amount (Area 3)			
DEM	73	-	56
Test	75	-	52
Error (%)	2.67	-	7.69

CHAPTER 4

EXAMINATION OF PARTICLE PROPERTIES' DURABILITY TO THERMAL CYCLING AND HIGH TEMPERATURES

4.1 Thermal Cycling and Particle Durability

Particles are expose to thermal cycling inside the operation cycle of a thermal power plant. They receive solar radiation, and they heat up to temperatures about 700-800 °C; they exchange heat and give their thermal energy to the thermo-cycle and cool down. This thermal cycle exposure can affect the bulk behavior if it affects particle' properties. To see if particle properties are affected by thermal cycling, the cycling process was replicated in the laboratory environment by utilizing a furnace. The discharge test was re-performed with thermally cycled particles and discharged mass, AOR and scattering amount were measured.

CarboHSP 40/70 particles were thermally cycled between room temperature and 700 °C. They were heated up to 700 °C inside a furnace. To ensure that particles reach the target temperature, they were kept at 700 °C for two hours. After that, the furnace was shut down and particles were exposed to room temperature air. One cycle was completed in 3-4 hours. This process was repeated 50 times for CarboHSP 40/70 and 20 times for sand.

One can see the comparison of thermally cycled and non-cycled CarboHSP 40/70 particles in Figure 4.1. No change was observed in the physical properties of particles like color, particle shape and size. Besides, particle and bulk density were measured and no change was recorded.

Figure 4.1: Comparison of non-cycled (left) vs cycled (right) CarboHSP 40/70 particles

Calibration measurements were repeated for 25 g of thermally cycled CarboHSP 40/70 particles. Discharge time and AOR results are within the measurement deviations. Moreover, to see the effect better, 50 g, 100 g and 150 g thermally cycled particles were tested against non-cycled particles at the same amounts. All of measurements with higher particle amounts are also within the measurement deviations of non-cycled particles. It was observed that particles do not agglomerate or crumble, and their sizes stay the same. This suggests that inter-particle friction coefficients are not affected by thermal cycling. Any particle shape change was not observed. This contributes to the finding that the rolling friction coefficient is not affected by thermal cycling. Moreover, any color change did not appear, which can relate to the particles' stable chemical structure. Thus, it can be said that material properties stayed the same, so the sliding friction coefficient. Scattering amount also coherent with non-cycled particles' scattering results. Unchanged particle shape, size, and weight might have affected this.

No significant changes in physical properties were observed. This proves that CarboHSP 40/70 particles are quite resistant to thermal cycling because it is a sintered material.

Figure 4.2: Comparison of cycled (left) vs non-cycled (right) sand particles

The color of sand particles changed after the first thermal cycle. However, no further color change was observed when the thermal cycling process was repeated. This color change might be an indication of a change in the chemical or crystal structure of the sand particles, such as the oxidation of some chemical component. The color change of the sand might alter the particles' optical properties, such as thermal absorptivity and reflectivity. Change in the optical properties of the particles affects the system's thermal performance. Moreover, any change on AOR, discharged mass and particle scattering measurement was not observed. This proves that after 20 cycles, particle properties of sand did not change. However, more thermal cycles can cause wear on the sand particles. This affects the particle size distribution and also can change the particle properties.

4.2 High Temperature Experiments

Particle-based heat tranfer/storage systems in power plants especially in CSPs operates between 300 °C and 800 °C. Thus, it should be investigated if investigated particle properties can be used at high-temperature models. The discharge test was repeated with hot CarboHSP 40/70 and sand particles to figure out if particle properties are changing with temperature or not. The discharge test setup funnel and its stand were insulated with ceramic wool insulation. Particles were heated in the laboratory furnace. 25 g of hot particles were discharged from 5 mm diameter orifice as in the room temperature test. AOR, discharged mass and scattering amount was measured. Firstly, particles that are at 300 °C were tested. The test was then repeated at varying temperatures with gradually increasing with 50 °C intervals up to 600 °C.

Any change in physical properties was not observed. However, color of sand particles changed at 300 °C. As mentioned in the previous section, color change might affect the optical properties of the sand particles. Discharged mass, AOR and scattering amount were not changed for both particle types. However, high-temperature tests were repeated less than room temperature tests, deviation in the high-temperature measurements are higher.

High-temperature calibration measurement showed that particle properties do not change with the temperature. This can be because particles were not expanded or fragmented with temperature; shape and mechanical properties were not affected by changing temperature. Thus, it is evident that CarboHSP 40/70 and sand particles in the related systems can be modeled with the same mechanical particle properties at elevated temperatures.

Thermal expansion up to 600 °C on the orifice hole is much smaller than the smallest particles in the discharge mass. Thus, it does not disturb the calibration measurement. However, one should note that at higher temperatures orifice hole might be expanded significantly. Thermal expansion on the orifice can affect the measurement result independent of change in the particle properties. The predicted results are an increase in the discharged mass, a decrease in AOR and an increase in the scattering amount regardless of the change in the properties.

CHAPTER 5

INVESTIGATION OF THERMAL PROPERTIES

Various thermal property measurement instruments utilize different methods available. Thermal property measurement approaches are mainly categorized as steady-state and transient methods. Steady-state methods are based on applying a constant heat flux from one side of the sample and measuring the temperatures through the sample length when the temperature distribution in the sample becomes steady-state. Thermal properties are calculated from the steady-state temperature difference in the sample. In the transient methods, a heat source produces a transient heatwave. This heatwave creates a transient temperature change in the sample and thermal properties are calculated from time-dependent temperature increase in the sample. Transient methods are advantageous since they do not require waiting for a steady-state condition; measurements can be performed quickly. In some transient methods, it is possible to measure power diffused into the sample so that both thermal conductivity k and diffusivity α can be measured precisely. Hotwire and hot strip methods are two examples of that, but they both require long samples. It is because measurement wire sensitivity is directly proportional to the resistance of the wire.

The hot disk is one of the adaptations of the transient measurement method and relies on the Transient Plane Source (TPS) method [56]. Sensor probes of the hot disk contain long wire in the shape of a thin spiral disk. Thus, it can be obtained reasonably high resistance of the wire in a compact form convenient to work with smaller samples. Hot Disk can measure thermal properties of various materials such as bulk solids, sheet metals, slabs, anisotropic materials, porous structures, one-dimensional materials, liquids, pastes and powders at a wide temperature range. Hot disk device can measure the k in the range of 0.005 - 1800 $\mathrm{W/mK}$, α from 0.1 to 1200 $\mathrm{mm^2/s}$, volumetric specific heat capacity C_v up to 5 $\mathrm{MJ/m^3K}$. Reproducibility for k is $\pm$ 2 %, for α is $\pm$ 5 % and for C_v is $\pm$ 7 % [57]. In this thesis, the thermal properties of particles that are candidates to be used as heat transfer and storage medium in thermal power plants like CSPs were measured from room temperature to elevated temperatures by using the TPS Hot Disk device.

5.1 Transient Plane Source Method: Hot Disk Equipment

The hot disk device acts as both a heat source and a heat sensor while measuring. The long wire in the form of a spiral delivers a known amount of power to the sample and measure the temperature increase of the spiral wire itself as a resistance thermometer. TPS method is a standardized method in ISO 22007-2 [58]. It is advantageous to measure thermal conductivity and specific heat capacity simultaneously without any calibration, a dependency of measured temperature difference, or contact agents. Hot disk equipment used in this thesis is shown in Figure 5.1.

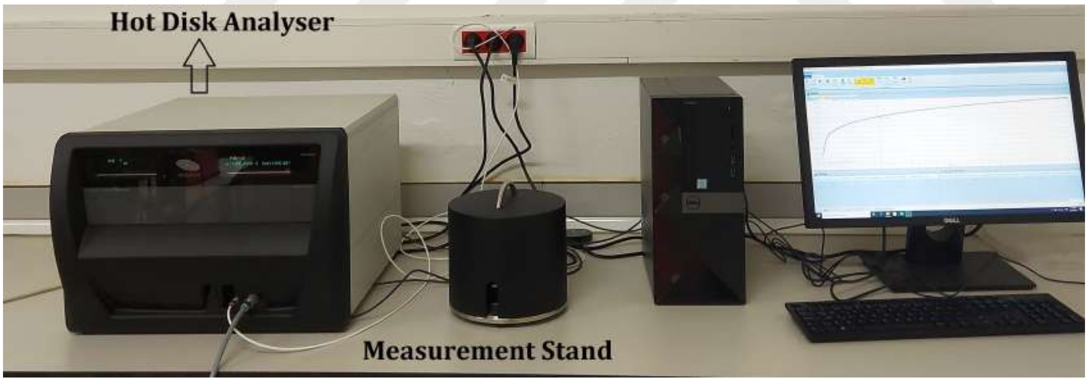

Figure 5.1: Hot disk equipment: computer, hot disk analyser and room temperature measurement stand

Assumptions that TPS theory applies are:

- Hot Disk sensor is composed of equally spaced concentric ring sources with an infinitely small ring width.

- The thickness and heat capacity of the sensor itself are neglected.
- Contact resistance between the sensor and the sample is neglected.
- Input power given to the sensor is step-wise.
- The sensor is located in the infinite medium.
- The contact interface between the sample and the sensor is flat and uniform.

Nickel spiral wire is covered by thin layers of insulating material made of Kapton or Mica. During measurement, the sensor is placed between two equal samples. Concentric rings act as a heat source and measurement sensor. The differential equation of heat conduction is solved numerically according to the temperature increase in the sensor, and thermal properties are calculated as follows [56]. An electrical pulse is given to the sensor and wire heats up, and thermometer resistance is increased as a function of time:

$$R(t) = R_0(1 + p(\Delta T_i + \Delta T_{samp}(\tau))) \tag{5.1}$$

R_0 is the initial resistance of the disk before a given electrical pulse. p is the temperature coefficient of the resistivity, τ is dimensionless time. ΔT_{samp} is the temperature increase of the sample surface touching the sensor. ΔT_i is the temperature difference between the sensor itself and the sample; in other words, a measure of thermal contact between the sensor of the sample. This difference becomes constant after a short time $\Delta \mathrm{t}_i = b^2/\alpha_i$. b is the thickness and α_i is the diffusivity of insulation material.

$$\Delta T_{samp}(\tau) = \frac{1}{p}(\frac{R(\mathrm{t})}{R_0} - 1) - \Delta T_i \tag{5.2}$$

The resistance of the sensor as a function of time is measured. The temperature increase in the sensor is calculated from Equation 5.2, and the temperature-time graph, which can be seen in Figure 5.2, is obtained.

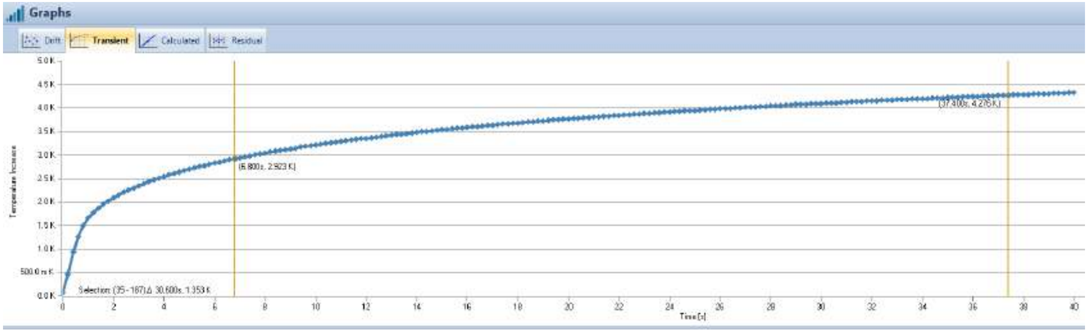

Figure 5.2: Transient measurement

After measurement by solving the differential equation of conduction, a numerical fit to measurement data is obtained. The calculated temperature increase is an input variable to the numerical fit to the temperature-time graph in Figure 5.2. This fit is computed according to the TPS theory (differential equation of conduction with concentric rings as heat sources), and dimensionless time-dependent temperature increase in the sample is obtained in the following:

$$\Delta T_{samp}(\tau) = \frac{P}{\pi^{(3/2)} r \mathrm{k}} F(\tau) \tag{5.3}$$

where r is the radius of the disk including the insulation, k is the thermal conductivity of the sample is being tested, P is the power given to the sample from the sensor, $F(\tau)$ is a function of dimensionless time.

Dimensionless time is explained as,

$$\tau = \sqrt{\frac{\mathrm{t}}{\Theta}} \tag{5.4}$$

t is transient measurement time and Θ is defined as characteristic time,

$$\Theta = \frac{\mathrm{r}^2}{\alpha} \tag{5.5}$$

α is the diffusivity of the sample.

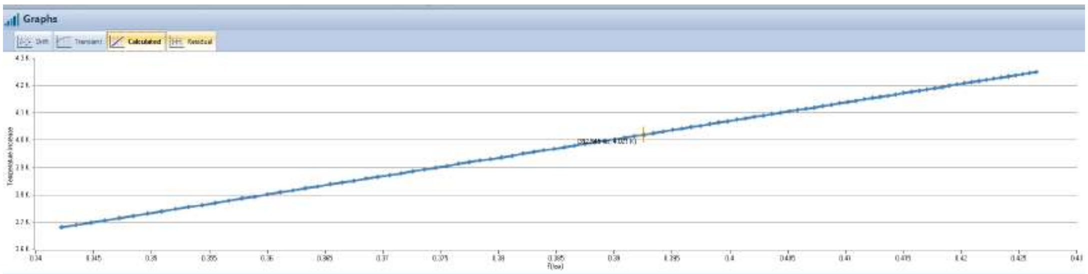

Figure 5.3: Numerical fit to transient measurement

Numerical integration is performed to calculate dimensionless time function by varying α with respect to dimensionless time, which is the upper limit of the integral of the $F(\tau)$ [56], [59]. The temperature increase as a function of the unitless time function is obtained as a straight line fit shown in Figure 5.3. The slope of the numerical fit is $\frac{P}{\pi^{(3/2)}\mathrm{rk}}$ (Equation 5.3). Thermal conductivity k of the sample is calculated by using this slope.

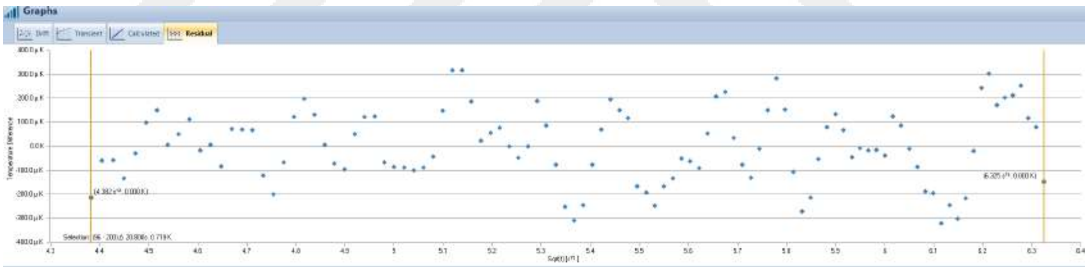

Figure 5.4: Residual graph

In order to make sure that measurement is right, residual of numerical fit and measured data is computed, as can be seen in Figure 5.4, and mean deviation is calculated. Specific heat capacity is obtained according to measured thermal conductivity and numerically estimated thermal diffusivity.

5.2 Measurements with Hot Disk

The heat penetration into the sample depends on the thermal properties of samples, so that transient measurement time and impulse power are given to the sensor should be adjusted accordingly. The thermal wave released from the sensor penetrates the sample based on the assumption that the sample is infinite. A boundary must be defined to limit the distance that thermal wave travels during the transient measurement time. Thus, the thermal wave does not exceed the edges of the sample, and measurement is performed just for the sample, not for the sample container or air environment. Probing depth Δd is defined as a boundary condition, which is the available shortest distance from the edge of the sensor to the sample boundary for both radial and axial directions. At the same time, the thermal wave speed in the sample depends on the thermal transport properties of the sample material. A numerical probing dept is calculated on the material property α and measurement time t, and it should not exceed the available probing depth Δd. Thus, the transient measurement time should be adjusted appropriately.

$$\Delta d = 2\sqrt{\alpha.\mathrm{t}} \tag{5.6}$$

Another critical point is adjusting the heating power applied to the sensor to generate a temperature increase. Typically 2-5 K total temperature increase in the measurement is suitable for accurate results. Temperature increase below 2 K is not enough for correct results. Besides, a high-temperature increase can damage the sensor. The thermal conductivity of the sample around the sensor limits the heating power P. If the sample is high thermal conductor material, high power can be applied without damage to the sensor. It is because high conductor material removes the heat energy from the sensor quickly. However, low conductivity materials do not handle high power, so low power input should be applied while measuring them.

To exclude contact resistance from the total measurement first part of the transient measurement graph, which appears as a sharp increase in the temperature, should not be taken into account. This increase can be seen easily in Figure 5.2.

To measure thermal properties at elevated temperatures tube furnace, integrated with the Hot Disk device, was used (Figure 5.5). Temperature resistive mica sensors were used at high temperatures. Mica sensors are designed for high temperatures, and they are compatible with the furnace. The mica sensor's thickness is 250 μm, while the kapton sensor thickness is 60 μm.

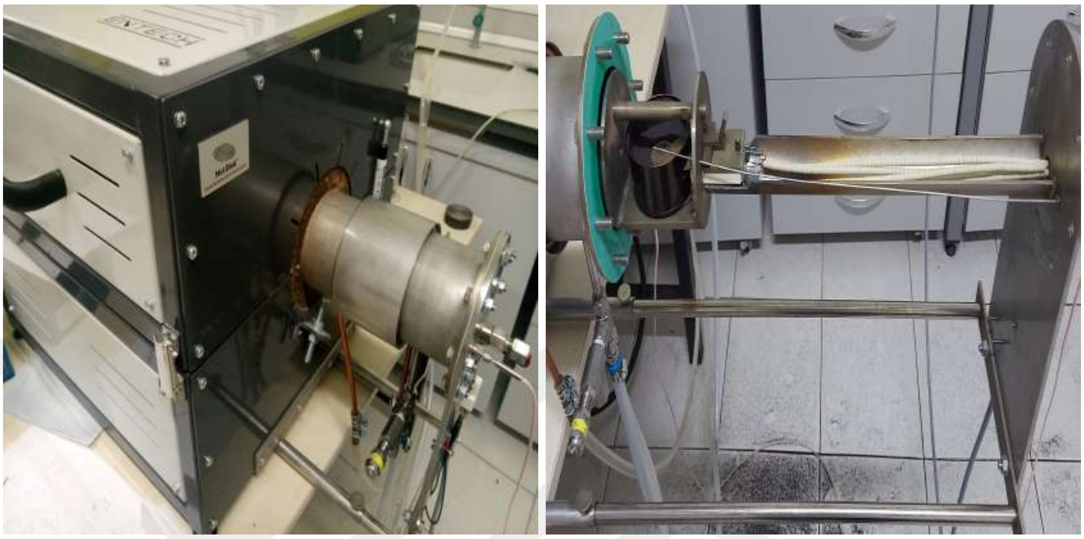

(a) Closed (b) Open

Figure 5.5: Tube furnace

Any temperature deviation should be avoided while performing transient measurement since the sensor can detect the small temperature differences. Stabilization of the furnaces' inside temperature takes a long time; thus, it was waited for 2-3 hours after reaching the target temperature value. Drift measurement was performed 40 seconds before the transient measurement to ensure that any temperature drift does not exist. A temperature drift graph is obtained, which must be scattered around the x-axis to avoid temperature drift.

While performing all of the measurements, these facts were considered for accurate results [57]:

- Temperature drift should be avoided.
- The transient plot should be continuous without any discontinuity or jumps.

- Total temperature increase should be greater than 2 K to perform the transient measurement and lower than 5.5 K for sensor accuracy. The power applied to the wire should be adjusted accordingly.
- Contact resistance should be excluded from calculations; this is possible by removing at least the first 10 measurement points.
- A computed graph of $\Delta T_{samp}(\tau)$ vs. $F(\tau)$ should be a perfectly straight line to get correct iterative results of thermal properties.
- Calculated probing depth should not exceed the sample boundaries not to measure the metal container.
- Mean deviation should be in the order of 10^{-5} or 10^{-4}, the order of 10^{-3} is a sign of a poor result.
- Residual data should scatter randomly around the horizontal axis.

By considering all of these factors, measurements were performed, 200 data were taken for each measurement. Appropriate power and measurement time were utilized according to the sample. All measurements were performed by using the isotropic measurement module. Each measurement was taken at least 3 times with 45 minutes intervals.

5.2.1 Room Temperature Measurements and Sensor Comparision

Measurement of properties of discrete medium like particle beds is a challenging task. Thus, sensor type, sensor size, and sample size should be chosen carefully. It should be noticed that the void fraction, particle size, isotropicity of the sample affect the measurement results.

Large measurement sensor is advantageous for low conducting porous materials. A larger sensor radius r means a long heater wire as a spiral, which reduces heat loss proportion from the sensor and increases the accuracy of measurements [60], [61]. Thus, the best practice is to use the biggest possible sensor. Meanwhile, the sample size should be in accordance with the sensor size. The transient thermal wave should not exceed the sample boundaries during the measurement time.

(a) Half filled holder (b) Filled holder

Figure 5.6: Experiment setup for particles with mica sensor in tube furnace

In this study, high-temperature measurements were performed in the tubular furnace. Inner dimensions of the tube furnace are limiting factors for sample and sensor size. The biggest possible custom-made sample holder was prepared to fit in the furnace. A sensor slot was opened on the holder, and it was filled with particles to insert the sensor between two equal samples (Figure 5.6). Ceramic wool insulation was placed on the slot's open parts to prevent the particles from poured from the sensor slot.

(a)

(b)

(c)

(d)

Figure 5.7: Measurement environment for sand particles measured by mica (a) and kapton (b) sensor, CarboHSP 40/70 particles measured by mica (c) and kapton (d) sensor

High-temperature measurements were performed by using a mica sensor. Firstly, two different sizes of mica and kapton sensors were compared at room temperature for stainless steel verification samples, CarboHSP 40/70 and sand particles. 9 mm and 6.5 mm radius sensors were chosen since they are most suitable for the maximum possible sample sizes of examined particles. Measurement environment was kept the same for proper comparison of kapton and mica sensors (Figure 5.7).

Table 5.1: Thermal conductivity and specific heat capacity measurement of stainless-steel verification samples with different sensors at room temperature

		Specific Heat (j/kgK)	**Error** (%)	**Conductivity** (W/mK)	**Error** (%)
	Literature Value	470.00		13.55	
Kapton	6.5 mm radius	437.42	6.93	13.19	2.66
	9 mm radius	459.78	2.17	13.60	0.37
Mica	6.5 mm radius	455.65	3.05	13.65	0.74
	9 mm radius	419.20	10.81	13.28	2.05

Table 5.1 compares the kapton and mica sensor measurements at room temperature for stainless steel verification samples. Different from measurement results of CarboHSP 40/70, stainless steel measurements do not differ for sensor insulation type or sensor diameter. The reason for that is stainless steel has high thermal conductivity and diffusivity compared to the CarboHSP 40/70.

Table 5.2: Bulk thermal conductivity and specific heat capacity measurement of CarboHSP 40/70 with different sensors and errors between literature values at room temperature

		Specific Heat (j/kgK)	**Error** (%)	**Conductivity** (W/mK)	**Error** (%)
	Literature Value	734.46		0.21	
Kapton	6.5 mm radius	813.95	10.82	0.24	10.86
	9 mm radius	751.55	2.33	0.21	1.79
Mica	6.5 mm radius	888.67	20.97	0.31	45.163
	9 mm radius	863.99	17.64	0.30	40.72

Table 5.3: Bulk thermal conductivity and specific heat capacity measurement of sand with different sensors at room temperature

		Specific Heat (j/kgK)	**Error** (%)	**Conductivity** (W/mK)	**Error** (%)
	Literature Value	-	-		-
Kapton	6.5 mm radius	382.87	-	0.31	-
	9 mm radius	459.33	-	0.32	-
Mica	6.5 mm radius	533.34	-	0.40	-
	9 mm radius	478.51	-	0.41	-

Table 5.2 shows that the kapton sensor's measurement results are in good agreement with theoretical literature values for CarboHSP 40/70 particles. As shown in Table 5.3, sand particle measurements have no error estimations because different types of sand have different thermal properties. Long measurement times were utilized while measuring particles because both the sample's conductivity is low, and a bigger sensor was used. The combination of long measurement time with the mica sensor's finite

thickness causes heat storage and diffusion in the sensor insulation material, temperature deviation between sensor and sample interface. These factors reduce the power into the sample and cause overestimation of thermal conductivity and heat capacity. Compare with low conductive samples, high thermal conductive materials do not require long measurement times. Their thermally conductive natures allow transient heatwave to diffuse in the sample in a very short time. Thus, heat diffusion and storage in the sensor insulation material and heat loss from the sensor interface reduces. This explains the accurate measurement by thick mica sensor for stainless steel verification samples. In addition, while the sensor's radius r increases for low conducting materials, error values are decreasing for thermal properties. This phenomenon is explained by the fact that a longer heater wire reduces the rate of heat loss from the sensor relative to the heat absorbed by the heater. This is not valid for stainless-steel verification samples because their thermal conductivity is high. Their high thermal conductive nature does not allow to heat loss from the sensor by absorbing the heat quickly. They can be measured with smaller sensors accurately. One can see in Tables 5.2 and 5.3 measurement deviation between the kapton and mica sensor is quite large. Mica sensor gives high measurement errors, even when the sensor size is large (Table 5.2). This case is explained by the mica sensor's finite thickness contradicting the sensor's no-thickness assumption in the TPS theory when measuring the low thermal conducting materials.

The findings in this thesis are consistent with the study of Zhang et al., who measured low, moderate, and high conductive samples by using both mica and kapton sensors. They concluded that the mica sensor overestimates the measurement results for the low thermal conductor materials with conductivity lower than 1.45 $\mathrm{W/mK}$. Their numerical study also showed that heat loss from the mica sensor is large compared to the kapton sensor, and it increases while sensor radius r decreases for low conducting samples [60]. Moreover, Zheng et al. compared extremely low conductive samples by measuring only the kapton sensor. They showed that for extremely low conductors, even the kapton sensor cause overestimation of the thermal properties [61]. This result agrees with a previous study by Zhang et al. for low conductivity materials [60]. They suggest a correction function for the measurement results of extremely low conductive materials by the kapton sensor [61].

5.2.2 High-Temperature Measurements and Sensor Bias Estimation

Measurement results of CarboHSP 40/70 and sand particles' bulk conductivity and specific heat capacity C_p can be seen in Figures 5.8 and 5.9. Measurements were performed with 100 °C intervals, maximum 400 °C for CarboHSP 40/70 and maximum 300 °C for sand particles could be reached. Above these temperatures, mica sensors failed. Mica sensors are composed of layers that are held together by glue. These layers separated at high temperatures since glue between layers failed. Mica sensors are supposed to resist up to 800 °C temperature. However, the used custom-made holder and tube furnace internal geometry does not allow to apply pressure on the sample so on the sensor. Thus, the sensor's layers are separated, and failure occurs. Mica sensor damaged at 500 °C for CarboHSP 40/70 and 400 °C for sand particles.

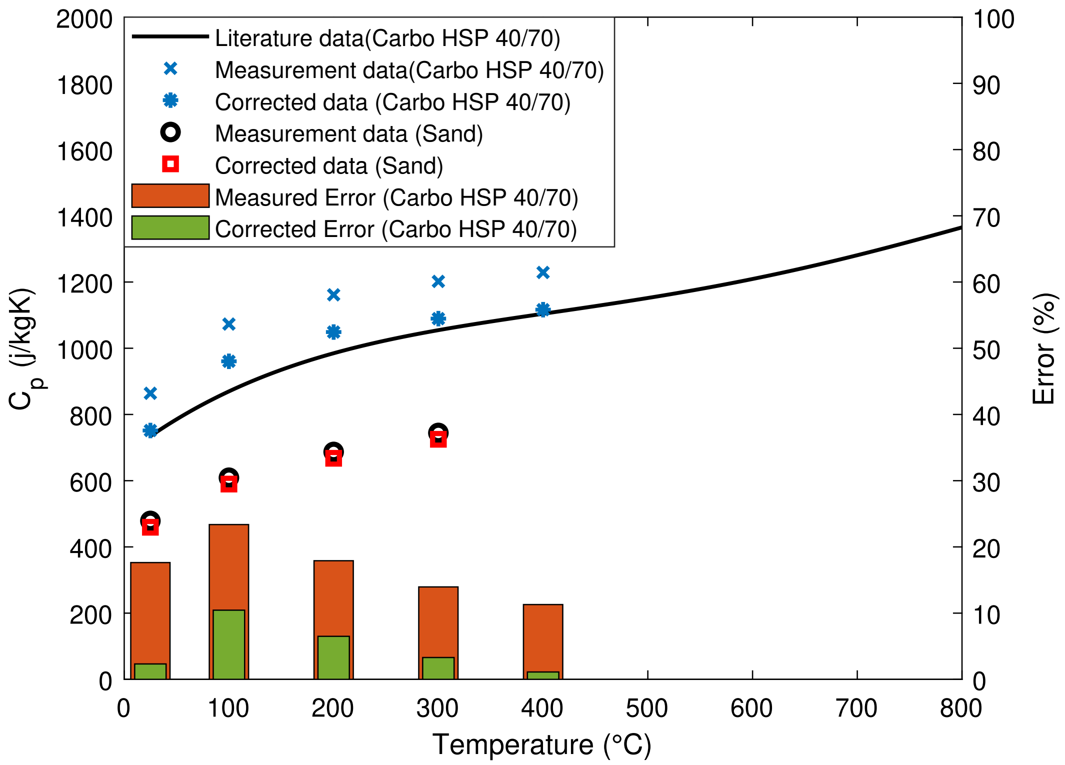

Figure 5.8: Measured and corrected results of specific heat capacity for sand and CarboHSP 40/70 and literature values for CarboHSP 40/70

As discussed in the previous section, measurement results are overestimated because of the high thermal mass of the mica insulated measurement sensors. The mica sensor's overestimated measurement results in this study were corrected according to the difference between the kapton and mica sensor measurement at room temperature. The measurement difference between the mica and kapton sensor at room temperature is assigned as an overestimation amount. It is subtracted from high-temperature measurement results, and sensor bias is corrected in this way.

Hot disk calculates the specific heat capacity in the volumetric form C_v. Since the literature value is given in the mass form, measured volumetric heat capacity is converted to mass heat capacity. Granular medium composed of air and solid particles, thus calculation of mass heat capacity is performed according to the rule of mixtures. Details can be found in Appendix A.

As mentioned in Chapter 1, there is only one available data on the specific heat capacity of CarboHSP 40/70 particles in the literature. C_p data of CarboHSP 40/70 in the literature mentioned in Figure 5.8 is a fitted polynomial to a DSC measurement by Siegel et al. [12]. Measurement errors were computed based on this data. Measurement and corrected results of C_p can be seen in Figure 5.8. One can notice that error values decreased dramatically with sensor bias correction. The error between literature value and corrected measurement values are maximum 10.45 $\%$. Multi-size particles are one of the reasons that cause the error. As mentioned in Section 3.1.1, the size of CarboHSP 40/70 varies from 208 μm to 724 μm. This multi-size nature of particles disrupts the isotropic structure of the sample. Moreover, deviations of the measured bulk density of the particles affect the results directly. Lastly, the literature value used as a reference in this study is a data fit to DSC measurement results but not actual measurement results, which is another source of error.

The only accurate measurement value in the literature for CarboHSP 40/70 particles is verified using Hot Disk TPS measurement. As shown in Figure 5.8, sand particles have a lower C_p than the CarboHSP 40/70. Higher specific heat is desired for both receiver and thermal storage applications for an efficient system. Although the sand is an economical alternative, it's C_p is nearly two times lower than the CarboHSP 40/70.

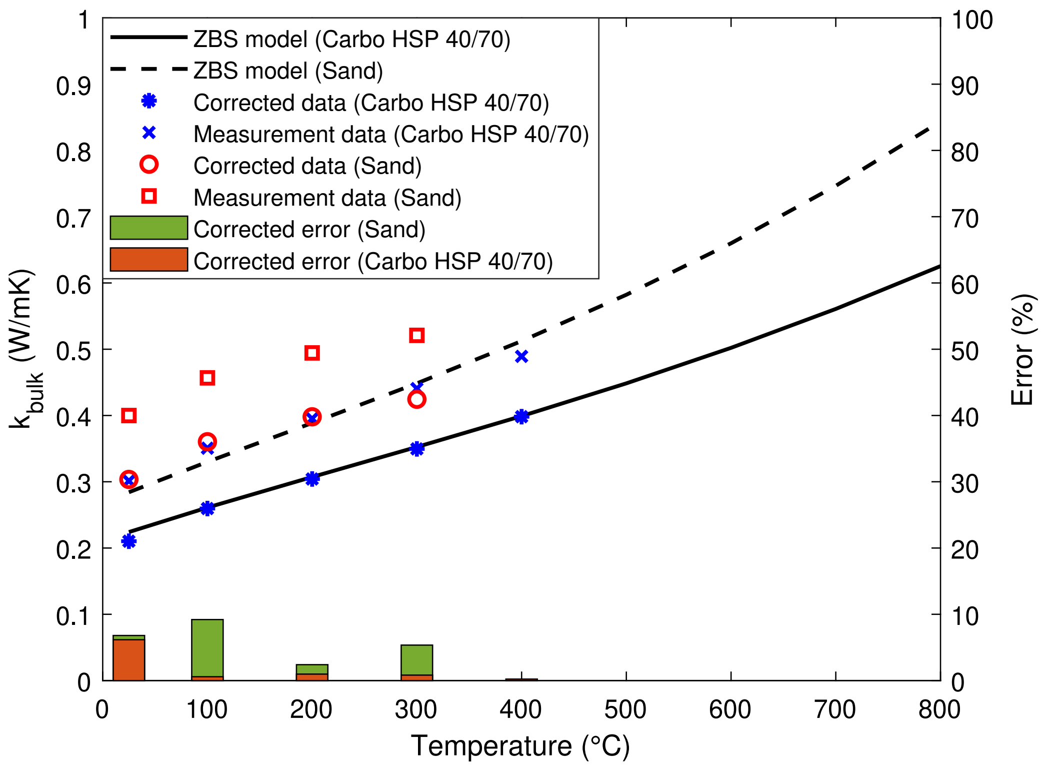

Figure 5.9: Measured and corrected results of bulk thermal conductivity and ZBS Model for sand and CarboHSP 40/70

ZBS model was utilized in this study to determine the accuracy of the bulk thermal conductivity of the measured particle medium of CarboHSP 40/70 and sand (Figure 5.9). Widely used ZBS model represents all of the heat transfer mechanism exist in particle beds [44]. According to the ZBS model, the particle beds' effective conductivity is affected by particle size, porosity, the thermal conductivity of particles, thermal properties of interstitial fluid, and temperature. Details of this model can be found in appendix B.

Mean diameters of particles were used for ZBS model (385 μm for CarboHSP 40/70 and 765 μm for sand). Thus size distribution function was set to 1 for both particle types. Particles' conductivity was inserted as 2 $\mathrm{W/mK}$ as given in the literature for CarboHSP 40/70 [7] and 1.5 $\mathrm{W/mK}$ for sand. Shape factor C_f was set to 1.25 for CarboHSP 40/70 and 1.40 for sand particles [44]. All measurements are performed on atmospheric pressure. Proper air thermal properties and density are inserted according to the increasing temperature.

Measurement results by hot disk dramatically decreased after sensor bias correction from $\sim 34\ \%$ to $\sim 6\ \%$ for CarboHSP 40/70; from $\sim 40\ \%$ to $\sim 9\ \%$ for sand. Sources of error for corrected measurement are as follows:

- The measured sample is composed of multi-size particles; this might reduce isotropicty of the bed.
- Particle bed sample might have different porosities in different locations of the bed.
- Particle conductivity value is taken as 2 $\mathrm{W/mK}$ [7] for all temperatures, which might vary according to the temperature. However, it should be noted that particle conductivity is the least influential factor of bulk conductivity according to the ZBS model.

Results show that CarboHSP 40/70 particles have lower $\mathrm{k_{bulk}}$ than sand particles. $\mathrm{k_{bulk}}$ is not as critical as the C_p for power plant design. However, high bulk thermal conductivity can be desired for some heat receiver types, such as dense granular receivers to conduct heat to interior parts. In addition, high $\mathrm{k_{bulk}}$ can be advantageous for some storage applications to extract heat easily.

CHAPTER 6

CONCLUSIONS

6.1 Concluding Remarks

Mechanical and thermal properties of CarboHSP 40/70 and sand particles were investigated in this study. An inclined plane test was used to determine the particle-wall friction coefficients. Since examined particles are small (mean size < 1 mm), it is not possible to observe the particles while they are sliding or rolling on the inclined metal plate. Thus, by utilizing the symmetric friction coefficient matrix, the inclined plane test was inverted. Particles were fixed as a surface by gluing them on a surface. The metal ball's rolling angle and sliding angle of the metal surface were measured and μ_{p-w} and $\mu_{r,p-w}$ was found.

Inverse calibration method was utilized to find particle-particle friction coefficients. The discharge test was modeled on DEM with possible different inter-particle friction coefficient pairs. Both μ_{p-p} and $\mu_{r,p-p}$ were calibrated by utilizing AOR and discharged mass measurements which are outputs of the discharged test. The μ_{p-p}-$\mu_{r,p-p}$ pair that match the real-life discharged mass and AOR measurement is the calibrated exact results.

A new measurement method for investigation of the restitution coefficient e_{p-p} and e_{p-w} is presented. The discharge test was utilized and the scattering amount of particles on a metal plate was measured. Particle scattering amount on the plate is both affected from e_{p-p} and e_{p-w} depending on the region of the plate. Thus, this test is fairly suitable for investigating the e_{p-p} and e_{p-w}.

Since particles are aimed to be used at high-temperature applications, particle properties were examined at high temperatures. Results confirmed that particles can be modeled at elevated temperatures with the obtained mechanical properties at room temperature. Moreover, particles undergo thermal cycling during their lifetime in related systems. In order to understand if particle behavior is changing after many thermal cycling, particles were thermally cycled and the mechanical property calibration test was repeated with them. Test results of AOR, discharged mass and scattering amounts did not change. This proves that the same particle properties will be valid after many thermal cycles in operation and particles will show the same bulk behavior.

Besides, the shape, size, density and color of CarboHSP 40/70 particles were not affected by high temperatures and thermal cycling. This proves that CarboHSP 40/70 particles are quite resistive to high temperatures and thermal cycling, appropriate for continuous heat transfer/storage applications. However, sand particles' color changed permanently with the heat effect. This may cause a change in the sand particles' optical properties, such as an increase in absorbtivity and a decrease in reflectivity.

Hot Disk equipment was used to measure the bulk thermal conductivity and heat capacity of particles. Heat capacity measurements of CarboHSP particles are pretty consistent with previous measurements performed by Siegel et al. on DSC [12]. C_p is the most critical parameter of the heat transfer medium of power production systems since it directly affects the system efficiency. CarboHSP 40/70 has a higher C_p value compared to sand. This makes CarboHSP 40/70 more advantageous to be used as a heat transfer medium. Measured $\mathrm{k_{bulk}}$ values of CarboHSP 40/70 and sand particles are compatible with ZBS model [44]. $\mathrm{k_{bulk}}$ value of sand is higher than $\mathrm{k_{bulk}}$ value of CarboHSP 40/70. Although high $\mathrm{k_{bulk}}$ is not a critical design parameter as high C_p, some application types might require high $\mathrm{k_{bulk}}$ such as dense granular receiver designs.

6.2 Future Work

In order to understand better the behavior of the particles as a working fluid/storage media in the systems following studies will be performed in the near future;

- More thermal cycling should be applied to particles to understand the effect on the real system.

- Thermal properties of thermally cycled particles should be measured.
- High-temperature calibration measurements should be conducted with proper equipment at higher temperatures.
- Components of a particle-based system such as particle receiver for CSP, particle storage system, particle HEX should be modeled with investigated particle properties.

REFERENCES

[1] S. Hess, *Solar Thermal Process Heat (SPH) Generation*. Elsevier Ltd, 2016.

[2] M. Diago, A. C. Iniesta, A. Soum-Glaude, and N. Calvet, "Characterization of desert sand to be used as a high-temperature thermal energy storage medium in particle solar receiver technology," *Applied Energy*, vol. 216, pp. 402–413, April 2018.

[3] A. Calderón, A. Palacios, C. Barreneche, M. Segarra, C. Prieto, A. Rodriguez-Sanchez, and A. I. Fernández, "High temperature systems using solid particles as TES and HTF material: A review," *Applied Energy*, vol. 213, pp. 100–111, March 2018.

[4] A. Katterfeld and C. Wensrich, "Understanding granular media: from fundamentals and simulations to industrial application," *Granular Matter*, vol. 19, no. 4, pp. 1–4, 2017.

[5] E. Karatairi and A. Ambrosini, "Improving the efficiency of concentrating solar power systems," *MRS Bulletin*, vol. 43, pp. 920–921, December 2018.

[6] C. Ho, J. Christian, D. Gill, A. Moya, S. Jeter, S. Abdel-Khalik, D. Sadowski, N. Siegel, H. Al-Ansary, L. Amsbeck, B. Gobereit, and R. Buck, "Technology Advancements for Next Generation Falling Particle Receivers," *Energy Procedia*, vol. 49, pp. 398–407, 2014.

[7] A. Calderón, C. Barreneche, A. Palacios, M. Segarra, C. Prieto, A. Rodriguez-Sanchez, and A. I. Fernández, "Review of solid particle materials for heat transfer fluid and thermal energy storage in solar thermal power plants," *Energy Storage*, vol. 1, no. 4, pp. 1–20, 2019.

[8] N. Siegel, M. Gross, C. Ho, T. Phan, and J. Yuan, "Physical Properties of Solid Particle Thermal Energy Storage Media for Concentrating Solar Power Applications," *Energy Procedia*, vol. 49, pp. 1015–1023, 2014.

[9] C. K. Ho, “A review of high-temperature particle receivers for concentrating solar power,” *Applied Thermal Engineering*, vol. 109, pp. 958–969, October 2016.

[10] T. Baumann and S. Zunft, “Properties of granular materials as heat transfer and storage mediumin CSP application,” *Solar Energy Materials & Solar Cells*, vol. 143, pp. 38–47, December 2015.

[11] Z. Ma, R. Zhang, and F. Sawaged, “Design of Particle-based Thermal Energy Storage for a Concentrating Solar power System,” in *Proceedings of the ASME 2017 11th International Conference on Energy Sustainability*, ES2017, 2017.

[12] N. P. Siegel, M. D. Gross, and R. Coury, “The development of direct absorption and storage media for falling particle solar central receivers,” *Journal of Solar Energy Engineering, Transactions of the ASME*, vol. 137, no. 4, 2015.

[13] T. Tan and Y. Chen, “Review of study on solid particle solar receivers,” *Renewable and Sustainable Energy Reviews*, vol. 14, pp. 265–276, January 2010.

[14] W. Wu, L. Amsbeck, R. Buck, R. Uhlig, and R. Ritz-Paal, “Proof of concept test of a centrifugal particle receiver,” *Energy Procedia*, vol. 49, pp. 560–568, 2013.

[15] A. C. Iniesta, M. Diago, T. Delclos, Q. Falcoz, T. Shamim, and N. Calvet, “Gravity-fed Combined Solar Receiver/Storage System Using Sand Particles as Heat Collector, Heat Transfer and Thermal Energy Storage Media,” *Energy Procedia*, vol. 69, pp. 802–811, may 2015.

[16] P. A. Cundall and O. D. L. Strack, “A discrete numerical model for granular assemblies,” *Géotechnique*, vol. 29, no. 1, pp. 47–65, 1979.

[17] C. González-Montellano, F. Ayuga, and J. Y. Ooi, “Discrete element modelling of grain flow in a planar silo: Influence of simulation parameters,” in *Granular Matter*, vol. 13, pp. 149–158, April 2011.

[18] S. M. Derakhshani, *Modelling dust liberation in bulk material handling systems*. PhD thesis, TU Delft University, 2016.

[19] M. Jahani, A. Farzanegan, and M. Noaparast, "Investigation of screening performance of banana screens using liggghts dem solver," *Powder Technology*, vol. 283, pp. 32–47, 2015.

[20] M. Combarros, H. J. Feise, H. Zetzener, and A. Kwade, "Segregation of particulate solids: Experiments and dem simulations," *Particuology*, vol. 12, no. 1, pp. 25–32, 2014.

[21] M. Marigo and E. H. Stitt, "Discrete element method (DEM) for industrial applications: Comments on calibration and validation for the modelling of cylindrical pellets," *KONA Powder and Particle Journal*, vol. 32, no. 32, pp. 236–252, 2015.

[22] Y. N. Chilamkurti and R. D. Gould, "Experimental and Computational Studies of Gravity-Driven Dense Granular Flows," in *Proceedings of the ASME International Mechanical Engineering Congress and Exposition*, 2015.

[23] Y. N. Chilamkurti and R. D. Gould, "Discrete element studies of gravity-driven dense granular flows in vertical cylindrical tubes," in *Proceedings of the ASME Power Conference*, 2016.

[24] R. Zanino, C. K. Ho, D. Romano, and L. Savoldi, "Preliminary discrete element modeling of a falling particle curtain for CSP central tower receivers," vol. 1734, no. 1, 2016.

[25] A. B. Morris, Z. Ma, S. Pannala, and C. M. Hrenya, "Simulations of heat transfer to solid particles flowing through an array of heated tubes," *Solar Energy*, vol. 130, pp. 101–115, 2016.

[26] M. Sandlin and S. Abdel-Khalik, "A study of granular flow through horizontal wire mesh screens for concentrated solar power particle heating receiver applications–part i:experimental studies and numerical model development," *Solar Energy*, vol. 169, pp. 1–10, 2018.

[27] M. Sandlin and S. Abdel-Khalik, "A study of granular flow through horizontal wire mesh screens for concentrated solar power particle heating receiver applications–part ii: Parametric model predictions development," *Solar Energy*, vol. 174, pp. 1252–1262, 2018.

[28] M. Sandlin and S. I. Abdel-Khalik, "An experimental and numerical study of granular flows through a perforated square lattice for central solar receiver applications," *Solar Energy*, vol. 174, pp. 463–473, nov 2018.

[29] V. Dreißigacker, S. Zunft, and H. Müller-Steinhagen, "A thermo-mechanical model of packed-bed storage and experimental validation," *Applied Energy*, vol. 111, pp. 1120–1125, 2013.

[30] N. Sassine, F. V. Donzé, B. Harthong, and A. Bruch, "Thermal stress numerical study in granular packed bed storage tank," *Granular Matter*, vol. 20, no. 3, pp. 1–15, 2018.

[31] C. J. Coetzee and R. G. Nel, "Calibration of discrete element properties and the modelling of packed rock beds," *Powder Technology*, vol. 264, pp. 332–342, 2014.

[32] H. Chen, Y. L. Liu, X. Q. Zhao, Y. G. Xiao, and Y. Liu, "Numerical investigation on angle of repose and force network from granular pile in variable gravitational environments," *Powder Technology*, vol. 283, pp. 607–617, October 2015.

[33] G. K. Barrios, R. M. de Carvalho, A. Kwade, and L. M. Tavares, "Contact parameter estimation for DEM simulation of iron ore pellet handling," *Powder Technology*, vol. 248, pp. 84–93, 2013.

[34] A. P. Grima and P. W. Wypych, "Investigation into calibration of discrete element model parameters for scale-up and validation of particle-structure interactions under impact conditions," *Powder Technology*, vol. 212, no. 1, pp. 198–209, 2011.

[35] C. Li, T. Honeyands, D. O'Dea, and R. Moreno-Atanasio, "The angle of repose and size segregation of iron ore granules: DEM analysis and experimental investigation," *Powder Technology*, vol. 320, pp. 257–272, October 2017.

[36] K. Senetakis, M. R. Coop, and M. C. Todisco, "The inter-particle coefficient of friction at the contacts of Leighton Buzzard sand quartz minerals," *Soils and Foundations*, vol. 53, no. 5, pp. 746–755, 2013.

[37] C. S. Sandeep, H. He, and K. Senetakis, "An experimental micromechanical study of sand grain contacts behavior from different geological environments," *Engineering Geology*, vol. 246, pp. 176–186, nov 2018.

[38] D. Kretz, S. Callau-Monje, M. Hitschler, A. Hien, M. Raedle, and J. Hesser, "Discrete element method (DEM) simulation and validation of a screw feeder system," *Powder Technology*, vol. 287, pp. 131–138, 2016.

[39] M. Ucgul, J. M. Fielke, and C. Saunders, "Three-dimensional discrete element modelling of tillage: Determination of a suitable contact model and parameters for a cohesionless soil," *Biosystems Engineering*, vol. 121, pp. 105–117, 2014.

[40] C. Coetzee, "Review: Calibration of the Discrete Element Method," *Powder Technology*, vol. 310, pp. 104–142, 2017.

[41] S. M. Derakhshani, D. L.Schott, and G. Lodewijks, "Micro– macro properties of quartz sand: Experimental investigation and dem simulation," *Powder Technology*, vol. 269, pp. 127–138, 2015.

[42] T. Roessler, C. Richter, A. Katterfeld, and F. Will, "Development of a standard calibration procedure for the DEM parameters of cohesionless bulk materials – part I: Solving the problem of ambiguous parameter combinations," *Powder Technology*, vol. 343, pp. 803–812, feb 2019.

[43] C. Kloss, C. Goniva, A. Hager, S. Amberger, and S. Pirker, "Models, algorithms and validation for opensource dem and cfd-dem," *Progress in Computational Fluid Dynamics An Int.*, vol. 12, no. 2/3, pp. 140 – 152, 2012.

[44] M. Neubronner and T. Bodmer, *VDI Heat Atlas*, ch. D6 Properties of Solids and Solid Materials, pp. 551–614. Berlin, Heidelberg: Springer Berlin Heidelberg, 2010.

[45] H. R. Norouzi, R. Zarghami, R. Sotudeh-Gharebagh, and N. Mostoufi, *Coupled CFD-DEM Modeling: Formulation, Implementation and Application to Multiphase Flows*. West Sussex: John Wiley & Sons, 2016.

[46] J. Horabik and M. Molenda, "Parameters and contact models for dem simulations of agricultural granular materials: A review," *Biosystems Engineering*, vol. 147, pp. 206–225, 2016.

[47] J. Ai, J. F. Chen, J. M. Rotter, and J. Y. Ooi, "Assessment of rolling resistance models in discrete element simulations," *Powder Technology*, vol. 206, 2011.

[48] A. Jensen, K. Fraser, and G. Laird, "Improving the precision of discrete element simulations through calibration models," *13th International LS-DYNA Users Conference*, 2014.

[49] M. Paulick, M. Morgeneyer, and A. Kwade, "Review on the influence of elastic particle properties on dem simulation results," *Powder Technology*, vol. 283, pp. 66–76, 2015.

[50] H. Q. Do, A. M. Aragon, and D. l. Schott, "A calibration framework for discrete element model parameters using genetic algorithms," *Advanced Powder Technology*, vol. 29, pp. 1393–1403, 2018.

[51] Z. Yan, S. K. Wilkinson, E. H. Stitt, and M. Marigo1, "Discrete element modelling (dem) input parameters: understanding their impact on model predictions using statistical analysis," *Comp. Part. Mech.*, vol. 2, p. 283–299, 2015.

[52] S. Lommen, D. Schott, and G. Lodewijks, "Dem speedup: Stiffness effects on behavior of bulk material," *Particuology*, vol. 12, pp. 107–112, 2014.

[53] K. Iwashita and M. Oda, "Micro-deformation mechanism of shear banding process based on modified distinct element method vol.109 pp.192–205," *Powder Technology*, 2000.

[54] E. Polat, "Experimental investigation of fludized bed to be used as solar thermal energy storage," Master's thesis, METU, August 2019.

[55] K. M. Mandich, *An Experimental Study of a Vertical Tube Gas-Fluidized Bed A*. PhD thesis, University of California, SAN DIEGO, 2010.

[56] S. E. Gustafsson, "Transient plane source techniques for thermal conductivity and thermal diffusivity measurements of solid materials," *Review of Scientific Instruments*, vol. 62, no. 3, pp. 797–804, 1991.

[57] Hot Disk AB, *Hot Disk Thermal Constants Analyser Instruction Manual*, 2018.

[58] "Plastics — Determination of thermal conductivity and thermal diffusivity — Part 2: Transient plane heat source (hot disc) method," standard, International Organization for Standardization, Switzerland, 2015.

[59] Y. He, "Rapid thermal conductivity measurement with a hot disk sensor: Part 1. Theoretical considerations," *Thermochimica Acta*, vol. 436, no. 1-2, pp. 122–129, 2005.

[60] H. Zhang, Y. Jin, W. Gu, Z. Y. Li, and W. Q. Tao, "A numerical study on the influence of insulating layer of the hot disk sensor on the thermal conductivity measuring accuracy," *Progress in Computational Fluid Dynamics*, vol. 13, no. 3-4, pp. 191–201, 2013.

[61] Q. Zheng, S. Kaur, C. Dames, and R. S. Prasher, "Analysis and improvement of the hot disk transient plane source method for low thermal conductivity materials," *International Journal of Heat and Mass Transfer*, vol. 151, 2020.

Appendix A

CALCULATION OF MASS HEAT CAPACITY OF GRANULAR MEDIUM

Rule of mixtures with k constituents:

$$\sum_{n=1}^{k} C_{p,mixture} = w_n.C_{p,n} \tag{A.1}$$

$$w_n = \frac{m_n}{m_{mixture}} \tag{A.2}$$

For particle bed with interstitial fluid is air,

$$C_{p,mixture} = \frac{m_{fluid}}{m_{total}} C_{p,fluid} + \frac{m}{m_{total}} C_p \tag{A.3}$$

mass of fluid m_{fluid} is negligable compared to particle mass m. Thus,

$$C_{p,mixture} = C_p \tag{A.4}$$

Volumetric heat capacity C_v is calculated as follows:

$$C_v = \rho_{bulk} C_p \tag{A.5}$$

where ρ_{bulk} is bulk density of the particle bed.

Appendix B

ZEHNER-BAUER-SCHLÜNDER (ZBS) MODEL

According to the unit-cell ZBS model, the relative bulk thermal conductivity of the particle bed λ_{bulk} is calculated as follows:

$$\lambda_{bulk} = \frac{\mathrm{k}_{bulk}}{\mathrm{k}_f} = \big(1-\sqrt{1-\psi}\big)\psi + \big[(\psi - 1 + \lambda_G^{-1})^{-1} + \lambda_{rad}\big] + \sqrt{1-\psi}\big[\varphi\lambda_p + (1-\varphi)\lambda_c\big] \tag{B.1}$$

k_{bulk} is bulk thermal conductivity of particle bed, k_f is the thermal conductivity of the interstitial fluid between particles, λ_{rad} is relative radiation coefficient and λ_p is relative particle conductivity, λ_c is relative core conductivity and φ is flattening coefficient which was set to 0.01.

$$\lambda_c = \frac{2}{N}\left\{\frac{B(\lambda_p + \lambda_{rad} - 1)}{N^2\lambda_p\lambda_G}\ln\frac{\lambda_p + \lambda_{rad}}{B[\lambda_G + (1-\lambda_G)(\lambda_p + \lambda_{rad})]} + \frac{B+1}{2B}\left[\frac{\lambda_{rad}}{\lambda_G} - B\left(1 + \frac{1-\lambda_G}{\lambda_G}\lambda_{rad}\right)\right] - \frac{B-1}{N\lambda_G}\right\} \tag{B.2}$$

$$N = \frac{1}{\lambda_G}\big(1 + \frac{\lambda_{rad} - B\lambda_G}{\lambda_p}\big) - B\big(\frac{1}{\lambda_G} - 1\big)\big(1 + \frac{\lambda_{rad}}{\lambda_p}\big) \tag{B.3}$$

$$B = C_f[(1-\psi)/\psi]^{10/9} f(\zeta) \tag{B.4}$$

C_f is the shape factor, ψ is porosity of the particle bed and $f(\zeta)$ is the distribution function.

$$\lambda_{rad} = \frac{\mathrm{k}_{rad}}{\mathrm{k}_f} = \frac{4\sigma}{2/\epsilon - 1} T^3 \frac{d}{\mathrm{k}_f} \tag{B.5}$$

where d is the particle diameter, T is the temperature of the particle bed, ϵ is the emissivity of the particles, σ is the Stefan–Boltzmann constant (5.67×10^{-8} $\mathrm{W/m^2K^4}$).

Pressure dependency of the particle bed thermal conductivity is expressed by λ_G;

$$\lambda_G = \frac{\mathrm{k}_G}{\mathrm{k}_f} = \big(1 + (l/d)\big)^{-1} \tag{B.6}$$

l is the modified mean free path of the interstitial gas molecules;

$$l = 2\frac{2-\gamma}{\gamma}\sqrt{\frac{2\pi \mathrm{R}T}{M}}\frac{\mathrm{k}_f}{\mathrm{P}(2.C_{p,g} - R/M)} \tag{B.7}$$

k_f is thermal conductivity of the interstitial fluid, R is universal gas constant (8.314 $\mathrm{J/molK}$), $C_{p,g}$ is the specific heat capacity, M is molecular weight of the gas, P is pressure. Accommodation coefficient γ is calculated as follows:

$$log(\frac{1}{\gamma} - 1) = 0.6 - \frac{1000/T + 1}{C} \tag{B.8}$$

$C = 2.8$ for air

If the interstitial fluid is not gas, then one can assume that $\mathrm{k}_G = 1$.